AGU PUBLICATIONS

JGR

Journal of Geophysical Research: Space Physics

RESEARCH ARTICLE

10.1002/2017JA024374

Influence of velocity fluctuations on the Kelvin-Helmholtz instability and its associated mass transport

Katariina Nykyri[1,2], **Xuanye Ma**[1,3], **Andrew Dimmock**[2], **Claire Foullon**[4], **Antonius Otto**[3], **and Adnane Osmane**[2]

[1]Center for Space and Atmospheric Research, Embry-Riddle Aeronautical University, Daytona Beach, Florida, USA, [2]Department of Electronics and Nanoengineering, School of Electrical Engineering, Aalto University, Espoo, Finland, [3]Geophysical Institute, University of Alaska Fairbanks, Fairbanks, Alaska, USA, [4]College of Engineering, Mathematics and Physical Sciences, University of Exeter, Exeter, UK

Key Points:
- The seed spectrum properties of magnetosheath velocity fluctuations have impact on the Kelvin-Helmholtz instability
- For larger-amplitude seed, KHI reaches the nonlinear stage sooner, and plasma transport starts earlier than for the smaller-amplitude seed
- Most plasma transport occurs for seed spectrum including the frequency close to theoretical fastest growing KH mode

Correspondence to:
K. Nykyri,
nykyrik@erau.edu

Citation:
Nykyri, K., X. Ma, A. Dimmock, C. Foullon, A. Otto, and A. Osmane (2017), Influence of velocity fluctuations on the Kelvin-Helmholtz instability and its associated mass transport, *J. Geophys. Res. Space Physics*, *122*, doi:10.1002/2017JA024374.

Received 17 MAY 2017
Accepted 20 AUG 2017
Accepted article online 19 SEP 2017

Abstract Kelvin-Helmholtz instability (KHI) and associated magnetic reconnection and diffusion processes provide plasma transport from solar wind into the magnetosphere. The efficiency of this transport depends on the magnetosheath and magnetospheric plasma and field properties at the vicinity of the magnetopause. Our recent statistical study using data from the Time History of Events and Macroscale Interactions during Substorms spacecraft indicates that the amplitude of the magnetosheath velocity fluctuations perpendicular to the magnetopause can be substantial. We have performed a series of local macroscale 2.5-dimensional magnetohydrodynamic simulations of the KHI during strongly northward interplanetary magnetic field and with the initial plasma parameters typical to the dayside magnetopause by perturbing the initial equilibrium with time-dependent perpendicular velocity field fluctuations. The effect of the single-mode and multimode seed spectrums at different frequencies and amplitudes is studied. The plasma transport in Kelvin-Helmholtz vortices is quantified. The results show that when large-amplitude, low-frequency seed velocity fluctuations exist in the magnetosheath, the resulting KH waves grow faster, get larger in size, and can transport more plasma through magnetic boundary, resulting in diffusion coefficient of the order 10^9 m^2/s. The relevance of these findings to the solar wind-magnetosphere coupling is discussed.

Plain Language Summary Solar wind is magnetized plasma that couples to the near-Earth magnetic environment due processes that occur at the boundary of the Earth's magnetic shield (the magnetopause) and shocked solar wind plasma (magnetosheath). Solar wind properties are highly variable, and coupling efficiency depends on these solar wind and resulting magnetosheath properties. Giant plasma waves, some 20,000–40,000 km in wavelength (so called Kelvin-Helmholtz waves), can be excited at the magnetopause by velocity shear. Like surfer waves in the ocean, these waves can break the Earth's magnetic shield and carry solar wind plasma through this magnetic barrier. The present paper shows that when large-amplitude, low-frequency seed velocity fluctuations exist in the magnetosheath, the resulting KH waves grow faster, get larger in size, and can transport more plasma through magnetic boundary.

1. Introduction

The solar wind coupling with the Earth's magnetosphere is not direct because its properties are altered at the bow shock and can be further modified by the in situ physical processes in the magnetosheath. Therefore, the magnetosheath state plays a crucial role in determining the proficiency of the mechanisms at the magnetopause that influence mass and energy loading of the magnetosphere.

The main processes responsible for the transport of energy, momentum, and mass through the magnetopause are magnetic reconnection [*Dungey*, 1961; *Sonnerup and Cahill*, 1967; *Russell and Elphic*, 1978], Kelvin-Helmholtz instability (KHI) [*Miura and Pritchett*, 1982; *Pu and Kivelson*, 1983; *Belmont and Chanteur*, 1989; *Otto and Fairfield*, 2000] and diffusive processes [*Fujimoto and Terasawa*, 1994; *Johnson et al.*, 1997; *Johnson and Cheng*, 2001; *Cowee et al.*, 2010].

The KHI is produced by the free energy available due to velocity shear between shocked solar wind and magnetospheric plasma. At low-latitude boundary layer it has been observed during northward interplanetary

magnetic field (IMF) [e.g., *Fairfield et al.*, 2000; *Hasegawa et al.*, 2004; *Lin et al.*, 2014], southward IMF [e.g., *Hwang et al.*, 2011; *Yan et al.*, 2014], and Parker spiral IMF [e.g., *Nykyri et al.*, 2006; *Moore*, 2012; *Moore et al.*, 2016] and at high latitude for dawnward or duskward IMF condition [*Hwang et al.*, 2012; *Ma et al.*, 2016]. A recent statistical study using data from the THEMIS (Time History of Events and Macroscale Interactions during Substorms) spacecraft observed Kelvin-Helmholtz waves ~19% of the time from all the magnetopause crossings [*Kavosi and Raeder*, 2015]. KHI has gained more interest during recent years because it has been shown to facilitate significant plasma transport across the magnetopause by producing magnetic reconnection as a secondary process [*Otto and Fairfield*, 2000; *Nykyri and Otto*, 2001; *Nykyri et al.*, 2003, 2006; *Hasegawa et al.*, 2009]. In two dimensions, the plasma transport occurring due to reconnection in KH vortices has been quantified using both MHD and Hall-MHD-based plasma models [*Nykyri and Otto*, 2001, 2004]. These results demonstrate that reconnection inside KH vortices can transport magnetosheath plasma into the magnetosphere with a transport velocity of ~1–2 km/s, corresponding to a diffusion coefficient of order 10^9 m^2/s. This rate is adequate in forming cold, dense plasma sheet during northward IMF conditions on the timescales observed by *Fujimoto et al.* [1998]. In its nonlinear stage, KHI can develop thin boundaries of the ion inertia scale [*Nykyri and Otto*, 2004], which enables additional transport via ion diffusion [*Cowee et al.*, 2010].

MHD simulations have shown that the fastest growing KH mode has a wavelength, λ, proportional to the shear flow layer thickness (Δ) $\lambda = (2-4)\pi\Delta$ [*Miura and Pritchett*, 1982]. The short-wavelength modes grow faster and saturate at smaller amplitude than long-wavelength modes. These small vortices can coalesce nonlinearly creating larger-scale vortices leading to an inverse cascade of wave power [*Winant and Browand*, 1974]. The 2-D ideal MHD study of the KHI by *Miura* [1997] showed that the large-scale vortices are created due to linear growth of the subharmonic modes. However, the 2-D MHD and particle-in-cell simulations of *Matsumoto and Seki* [2010] indicate that significantly larger growth of subharmonics occurs when a broad spectrum of subharmonics is included. *Matsumoto and Seki* [2010] show that rapid formation of a broad plasma turbulent layer can be achieved by forward and inverse energy cascades of the KH instability. The forward cascade is triggered by growth of the secondary Rayleigh-Taylor instability excited during the nonlinear evolution of the KH instability. The formation of secondary instabilities (secondary KH and Rayleigh-Taylor instability) is driven by the centrifugal force of the rotating fluid, leading to a broad mixing layer [*Matsumoto and Hoshino*, 2004, 2006; *Nakamura et al.*, 2004; *Cowee et al.*, 2009, 2010]. These processes rapidly broaden the boundary layer and transport mass, momentum, and energy across the boundary.

The cold-component dawnside plasma sheet ions are hotter and denser by 30–40% when compared to the duskside [*Wing et al.*, 2005], which is indicative of the asymmetry in the entry mechanism or in the magnetosheath source plasma or both. However, statistically, the ion temperatures downstream of the quasi-parallel shock are only about 15% higher than downstream of the quasi-perpendicular shock [*Dimmock et al.*, 2015], which is not sufficient for explaining the level of asymmetry present in the plasma sheet. Ion gyroradius-scale waves also exhibit dawn-favored asymmetry at the magnetopause, which could generate additional heating and transport [*Yao et al.*, 2011].

It is well known that foreshock and magnetosheath downstream of the quasi-parallel shock are abundant with various plasma wave modes [*Eastwood et al.*, 2011, 2003, 2004, 2005; *Blanco-Cano et al.*, 2006]. *Dimmock et al.* [2014] showed that the amplitude of magnetic field fluctuations in the range of 0.1–2 Hz in the dayside magnetosheath is larger on the quasi-parallel (dawn) flank during a Parker spiral IMF orientation, while during southward IMF there is no clear dawn/dusk asymmetry. The fluctuation amplitude is also enhanced for periods of fast solar wind conditions [*Dimmock et al.*, 2014]. This strongly suggests that the IMF orientation and prevailing upstream shock geometry play crucial roles in dictating the magnetosheath fluctuation properties. These fluctuations and waves may directly impact magnetosheath plasma heating via wave particle interactions [*Dimmock et al.*, 2015] and also indirectly by exciting macroscopic KHI more easily on the flank where the seed fluctuation amplitude is larger. Also, the smaller magnetic field line tension occurs statistically in the dawn flank magnetopause [*Dimmock and Nykyri*, 2013], which makes KHI growth slightly faster at the dawn flank according to MHD simulations [*Nykyri*, 2013]. The study by *Taylor et al.* [2012], which observed more KH events at the dusk flank, is not in contrast with these results, because for many of their events the horizontal IMF was in the ortho-Parker spiral orientation, generating smaller magnetic field tension at the dusk magnetopause when compared to the dawn sector.

The Kelvin-Helmholtz waves are important not only for plasma transport but also for causing ultralow frequency (ULF) magnetospheric pulsations [e.g., *Claudepierre et al.*, 2008]. The continuous ULF pulsations according to *Jacobs et al.* [1964] are classified in five categories: 0.2–5 Hz (Pc1), 0.1–0.2 Hz (Pc2), 22–100 mHz

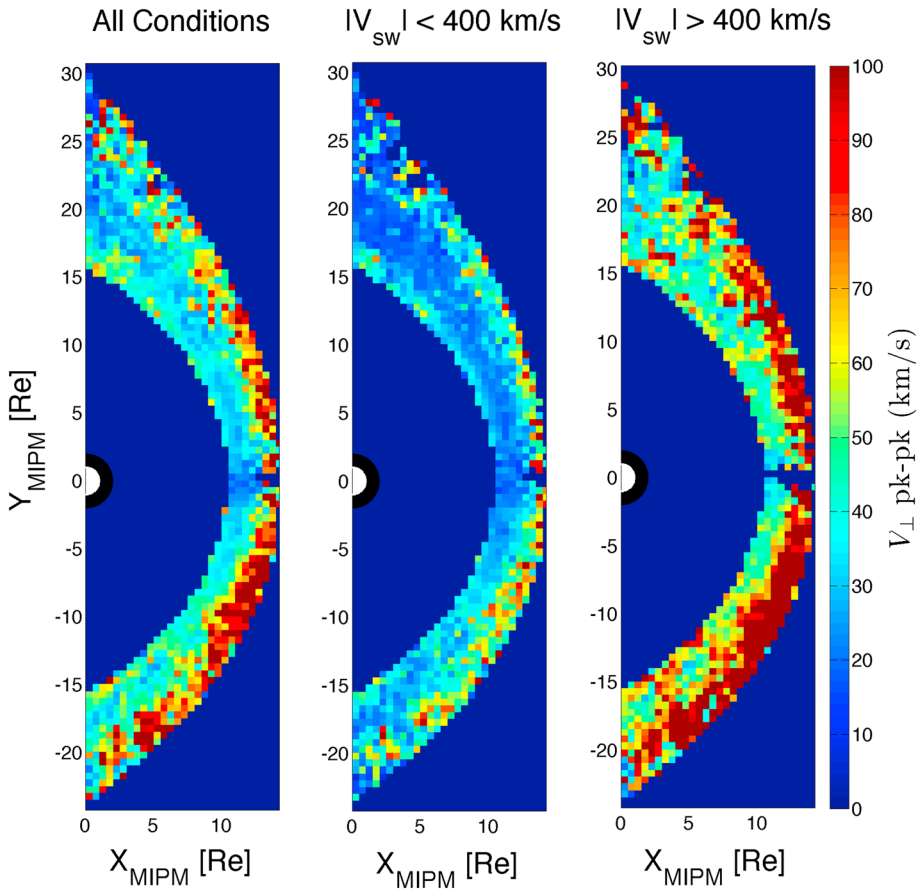

Figure 1. Statistical maps presenting 7 years of THEMIS measurements of the mean peak-to-peak amplitude of perpendicular velocity fluctuations in the magnetosheath interplanetary medium (MIPM) reference frame for (left) all, (middle) fast, and (right) slow solar wind. The "perpendicular" fluctuation is defined with respect to the average magnetosheath flow vector for each THEMIS 3 min data interval. Because the average flow in the magnetosheath is closely tangential to the closest, local magnetopause boundary, these fluctuations can be approximated as being perpendicular to the local magnetopause. The details of the frame and data processing can be seen in Appendix A.

(Pc3), 7–22 mHz (Pc4), and 2–7 mHz (Pc5). The fastest growing KHI has an angular frequency of $\omega \approx v_{shear}/2\Delta$, where Δ is the velocity shear layer thickness [*Miura and Pritchett*, 1982]. This coincides with Pc3–Pc5 range geomagnetic fluctuations. It has been shown that the Pc5 power statistically favors dawn sector magnetopause [*Nosé et al.*, 1995; *Nykyri and Dimmock*, 2016]. The toroidal mode Pc5-range ULF oscillations are fundamentally important as they can accelerate electrons at the radiation belts [*Elkington et al.*, 1999].

The magnetospheric ULF fluctuations can be also produced by dynamic pressure variations of the solar wind [*Korotova and Sibeck*, 1995; *Matsuoka et al.*, 1995; *Kepko et al.*, 2002; *Kepko and Spence*, 2003]. *Claudepierre et al.* [2010] studied the effect of idealized ULF dynamic pressure fluctuations embedded in the upstream solar wind in a global MHD simulation [*Lyon et al.*, 2004]. Authors concluded that the monochromatic solar wind dynamic pressure fluctuations can generate toroidal mode field line resonances where the upstream frequency matches a local field line eigenfrequency. A similar technique has been used by *McGregor et al.* [2014], who studied the effect of the Alfvénic solar wind fluctuations on the magnetosphere. Their results indicate that the solar wind Alfvénic fluctuations enhance low-frequency perturbations along the flanks and generate ULF waves in the dayside magnetosphere. Recently, *Osmane et al.* [2015] statistically demonstrated that for both northward and southward IMF, the IMF fluctuations with high power in B_z component produce greater level of geomagnetic activity on timescales consistent with viscous processes, such as KHI.

Usually, in local simulations the linear growth of the KHI is studied by applying a small incompressible spatial velocity perturbation (of ≈1–2 km/s) to the initial equilibrium [*Chen et al.*, 1997]. Most of the KH studies cited above study the evolution of the single KH mode and use a spatially confined time-independent

incompressible velocity perturbation of the order of 1–2 km/s. However, *Matsumoto and Seki* [2010] studied the effect of a continuous, spatial velocity perturbation spectrum including the fastest growing KH mode as well as its higher and lower harmonic modes. Their simulations showed that the inverse cascade is accomplished by nonlinear mode couplings among the KH unstable modes. While the fastest growing mode obeyed the linear growth rate, the growth rate of the longest wavelength allowed in the system was larger than expected from linear growth due to the mode couplings between the higher harmonic modes.

Figure 1 presents a statistical map of magnetosheath velocity fluctuations as measured by THEMIS spacecraft constellation. As illustrated by a statistical study in Figure 1 (see caption for details), the velocity fluctuations perpendicular to the magnetopause in the magnetosheath can be substantial: 20–50 km/s for slow ($V_{sw} < 400$ km/s) and 40–80 km/s for the fast ($V_{sw} > 400$ km/s) solar wind, respectively. This motivates us to investigate in detail the impact of a more realistic magnetosheath velocity spectra on the dynamics of the KHI. In this present paper, we investigate how the amplitude and frequency of the magnetosheath seed velocity perturbations affect KHI and associated plasma transport during strongly northward IMF by using local macroscale MHD simulations. The presented results suggest that there is a causal link between the solar wind/foreshock fluctuations and magnetospheric dynamics resulting from varying development of the KHI in terms of magnetosheath driver frequencies and the dayside flank velocity shear layer thickness.

The paper is organized as follows. Section 2 describes the methodology: simulation setup with the time-dependent velocity fluctuations perpendicular to the magnetopause and the method for quantifying the plasma transport produced by magnetic reconnection in the KH vortices. Section 3 describes the results: (a) evolution of the KHI due to single-mode seed fluctuations with a smaller (CASE 1) and larger (CASE 2) amplitude, (b) comparison of the KHI dynamics due to multimode seed fluctuations with a different amplitude for each mode (CASE 3), and (c) study of the effects of the initial random phase. In section 4 we conclude, and finally, in section 5 we discuss the relevance of the findings for the solar wind-magnetosphere coupling and possible links to the radiation belt dynamics.

2. Methodology

2.1. Macroscale MHD Simulations

The evolution of the KHI is studied in the x, y-plane (nearly equatorial plane for strongly northward IMF) with well-tested 2.5-dimensional high-resolution MHD model [*Otto*, 1990; *Chen et al.*, 1997; *Otto and Fairfield*, 2000; *Nykyri and Otto*, 2001; *Nykyri et al.*, 2006; *Nykyri*, 2013]. The simulation results are presented in the coordinate system where x is along the magnetosheath flow, y is along the velocity gradient and normal to the uperturbed magnetopause, and z is perpendicular to x, y-plane. The initial configuration for the simulation uses a magnetic field of $b_{x0}(y) = b_0(y)sin\varphi$, $b_{y0}(y) = 0$, and $b_{z0}(y) = b_0(y)cos\varphi$ such that $90^\circ - \varphi$ is the angle between the **k** vector of the KH mode and the initial background magnetic field. For all the runs presented in this study we use $\varphi = 5^\circ$, which corresponds to a strongly northward IMF orientation. Simulation parameters in the magnetosheath (MSH), magnetospheric (MSP) side, and their normalization are shown in Table 1.

The simulation length scale, $L_0 = 600$ km, is set to a typical magnetopause thickness at the dayside [*Berchem and Russell*, 1982]. The simulation time, $t_0 = 5.8$ s, is the time it takes for an Alfvén wave to propagate the distance L_0 with a speed of $B_0/\sqrt{\mu_0 m_p n_0} = 103$ km/s. The velocity shear layer thickness, Δ, is set to $3L_0 = 1800$ km [*Paschmann et al.*, 1993]. Due to various temporal and spatial scales involved in this study, we test the effect of the periodic (CASES 1A, 1B, 2A, 2B, 3, and 4) and open (CASES 1C and 2C) boundary conditions along the shear flow direction, as well as the effect of different numerical resolutions. Simulations use fixed boundary conditions in y direction (perpendicular to the initial current layer). In order to avoid mode interaction when using periodic boundary conditions and effects of the wave reflection, we use a macroscale system with $[y, x] = 800 \times 400\ L_0$ corresponding to a box length of $\sim 38\ R_E$ and a larger system size of $\sim 76\ R_E$ perpendicular to the initial current layer. The simulations use an adjustable grid along y direction and fixed grid separation along x direction. All simulations use 803 grid points in y direction with the maximum resolution reaching 0.1 in the vicinity of the initial boundary separating magnetosheath and magnetospheric plasma. This resolution corresponds to a 60 km spatial resolution with our choice of L_0. CASES 1A, 2A, 3, and 4 use 803 grid points along shear flow direction (x), and CASES 1B, 1C, 2B, and 2C use 1603 grid points along x. Initial plasma and magnetic field profiles (density, pressure, velocity, and magnetic field) on the magnetosheath and magnetospheric side are set to typically observed values (based on statistical THEMIS data) at the dayside magnetopause between the subsolar point and the terminator. Unlike the studies cited above, the simulations presented in this paper

Table 1. Initial Conditions in Magnetosheath (MSH) and Magnetosphere (MSP) With Normalization

Parameter	MSH	MSP	Normalization
B	1.5	1.0	$B_0 = 15$ nT
n	1.5	0.5	$n_0 = 10$ cm^{-3}
p	3.55	4.8	$p_0 = 0.0895$ nPa
beta	1.58	4.8	
v_A	1.22	1.41	$v_0 = 103$ km/s
v_S	1.40	2.82	v_0
v_F	1.86	3.15	v_0
v_{shear}	1.5	0	v_0

are done in the magnetospheric inertial frame. The velocity at the magnetospheric side of the simulation is set to zero and gradually (with hyperbolic tangent profile) reaches the maximum shear flow, $v_{\text{shear}} = 1.5$ value at the magnetosheath side, corresponding to a 155 km/s shear flow.

We study the impact of the following time-dependent velocity fluctuations, $\delta v_y(t)$, perpendicular to the magnetopause at the upstream boundary (at $x = -200$) on the magnetosheath side of the simulation box to mimic the dayside magnetosheath fluctuations.

$$\delta v_y(t) = v_1 \sqrt{\frac{2}{N}} \sum_i^N \sin(2\pi f_i t + \phi_i) \tag{1}$$

Here N denotes the number of modes, f_i is the frequency of the mode, and ϕ_i is the random phase. Note that since this type of initial perturbation is not incompressible and we have a finite simulation box size, we study the evolution of the system only up to 150 Alfvén times which corresponds to $\approx$ 14.5 min. This minimizes the effects of reflection of compressional waves from the system boundaries as typical fast mode MHD waves (using the fast mode speed of 258 km/s, which is the average for simulation parameters obtained from both sides of the velocity shear layer) propagate a distance of $\approx$35 R_E in 14.5 min in the simulation domain.

First, we study the influence of monochromatic (single mode, $N = 1$) fluctuations with two different perturbation amplitudes, $v_1 = 0.0625$ (CASE 1), and second, $v_1 = 0.25$ (CASE 2) at seven different frequencies: 0.5, 1, 2, 3, 4, 8, and 15 f_{fg}, where $f_{\text{fg}} \sim v_{\text{shear}} k_{\text{fg}}/2\pi$ corresponds to the theoretical frequency of the fastest growing KH mode, where k_{fg} is set to $1/(2\Delta)$ in agreement with *Miura and Pritchett* [1982]. The normalized frequency of the fastest growing mode is thus $f_{\text{fg}} = 0.0398$ $f_0 = 6.86$ mHz, where $f_0 = 1/t_0$. The seed fluctuations thus consist of the following seven frequencies: (1) 3.44, (2) 6.86, (3) 13.7, (4) 20.6, (5) 27.4, (6) 54.9, and (7) 102.9 mHz. Using the classification by *Jacobs et al.* [1964], these seven frequencies correspond roughly to Pc5 (1, 2), Pc4 (3, 4), Pc3 (5, 6), Pc2 (7) frequency bands. In normalized units and with the factor of $\sqrt{2}$ the maximum perturbation amplitudes correspond to 9.15 km/s and 36.6 km/s perpendicular (to mean flow) fluctuations in the magnetosheath velocity for CASES 1 and 2, respectively. The same initial phase, $\phi_1 = 6.27$ rad (not exactly 2π), which was chosen by random number generator, was used for the single mode CASES 1 and 2.

Third (CASE 3), we study the multimode ($N = 2$–10) velocity fluctuations with equally spaced frequency intervals at the continuum range of 0.5–15.0 f_{fg} (Pc5–Pc2), respectively.

$$\delta v_y(t) = v_1 \sqrt{\frac{2}{\sum_i^N A_i^2}} \sum_i^N A_i \sin(2\pi f_i t + \phi_i) \tag{2}$$

For example, if $N = 5$, then the frequency interval is d$f = 3.625$ f_{fg} and $f_i = [0.50, 4.125, 7.75, 11.375, 15.0]$ f_{fg}. As in typical magnetosheath spectra the low- (high-) frequency fluctuations have higher (lower) amplitudes; we study the interaction of modes ($N = 2$–10) with different amplitudes ($A_i = 0.25/i$). The factor of $\sqrt{\frac{2}{\sum_i^N A_i^2}}$ in equation (2) ensures that the maximum multimode fluctuation amplitudes are roughly the same as those of the single modes, as there might be constructive interference between the modes. We use the same Fortran random number seed and generator for setting the initial phases for each multimode run. For mode $i = 1$, the same initial phase, $\phi_1 = 6.27$ rad, was used as for the single mode CASES 1 and 2. For the $N = 2$ case, $\phi_1 = 6.27$ rad and $\phi_2 = 3.56$ rad. For $N = 3$, $\phi_1 = 6.27$ rad, $\phi_2 = 3.56$ rad, and $\phi_3 = 6.07$ rad. For $N = 10$, $\phi_1^{10} = [6.27, 3.56, 6.07, 4.70, 2.31, 3.02, 0.46, 0.03, 2.18, 2.15]$ rad.

Fourth (CASE 4), we study and compare the effect of the four different initial phases, ϕ = [1.56, 3.13, 4.70, 6.27] (separated by multiples of $\pi/2$ from $\phi_1 = 6.27$) on single-mode fluctuations with $v_1 = 0.0625$. We also compare the effect of the initial phase for the multimode case, $N = 5$, by changing ϕ_1 from 6.27 rad to 1.56 rad.

2.2. Plasma Transport Quantification

The plasma transport in the present simulations is due to the same mechanism as presented in *Nykyri and Otto* [2001, 2004] and occurs because KHI twists the initially parallel magnetic fields in the shear flow plane, thus generating antiparallel fields that generate strong current layers both in the magnetosheath and magnetospheric side of the vortex. All runs use the same current-dependent resistivity value $\eta = 0.005$ and critical current density of 1.0 (in simulation units). Resistivity is turned on when critical current density is exceeded. Because reconnection dynamics is strongly driven by the inertia of the vortex motion, the details of the resistivity model do not have much effect on the results [*Nykyri and Otto*, 2001]. The same 2-D reconnection dynamics is also present in 3-D, but in 3-D additional effects (high-latitude double reconnection above and below the maximum velocity shear layer) come into play [*Faganello et al.*, 2012; *Ma et al.*, 2015] that will allow transport of high-density plasma blobs into the closed magnetospheric field lines. The transport in 2-D is due to a capture of high-density magnetic islands into the magnetospheric side. Sometimes, also low-density magnetospheric plasma can be lost into the magnetosheath. Here we only quantify the transport of high-density plasma into the magnetosphere, which is the dominant process. The direction of plasma transport in 2-D is dictated by the competition between density and current density asymmetry. If the current densities in the magnetosheath and magnetospheric side of the vortex are the same, the reconnection first occurs in the current layer with the higher plasma density, typically leading to transport of high-density, magnetosheath material into the magnetosphere (at the ionopause of Venus and Mars this may be reversed because ionosphere has higher density than the sheath plasma). In 2-D, and with initially antiparallel magnetic field geometry across the velocity shear layer, KHI can also produce reconnection directly between magnetosheath and magnetospheric fields [*Nykyri et al.*, 2006; *Nakamura et al.*, 2006; *Eriksson et al.*, 2016]. *Taylor et al.* [2008] showed strong observational evidence suggesting that KHI was the dominant process for cold dense plasma sheet formation at tail flanks, while high-latitude reconnection can play significant role at the dayside boundary layer.

Plasma transport is quantified in detail for CASES 1, 2, 3, and 4 in similar way as in *Nykyri and Otto* [2001] by calculating the mass of the magnetic islands (flux ropes) captured from the magnetosheath. The island boundaries are defined by plasma fluid elements which are used as tracers for the initial boundary. In two dimensions Ohm's law can be written as

$$\frac{\partial A_z(t)}{\partial t} + (\mathbf{V}\cdot\nabla)A_z(t) = -\eta J_z \tag{3}$$

A_z is the z component of the magnetic vector potential and changes along the path of a fluid element only due to the resistive term on the right side if the initial gauge of A_z is maintained. Boundary location is then computed based on value of $A_{z0} - \int_0^t \eta J_z dt$ using the fluid elements.

The results are expressed in terms of an average mass entry velocity

$$v_{\text{entry}} = \frac{\Delta M}{\Delta t}\frac{1}{\rho_{\text{sh}} L_x} \tag{4}$$

where $M = A\rho$ is the mass of the magnetic island (computed from the area and average plasma density of the island), Δt is the simulation time, L_x is the approximate length of the KH wave train, which is conservatively set to 100 L_0, and ρ_{sh} is the magnetosheath density. Note that in *Nykyri and Otto* [2001] L_x was set to the KH wavelength. Here (due to time-dependent initial perturbation) more than one wave can develop, and the wavelength for different initial seed spectrum is not constant. Thus, it is more reliable to compare the results between different cases by studying the transport over a constant length of 100 $L_0 = 9.4\ R_E$. For each simulation, v_{entry} was computed as a function of time for every 5.8 s. The maximum value of v_{entry} was collected during the first 14.5 min of the simulation and is denoted as v_{max} together with the corresponding time, t_{mmax}. The time when v_{entry} first exceeds a nonzero value is collected and denoted as t_{m0}.

Frequency, amplitude, and phase of the seed spectrum, as well as numerical resolution and boundary conditions along the shear flow, all have some effect on the net plasma transport rates. To study these dependencies systematically, we have simulated each single-mode case with two different numerical resolutions, amplitudes, and two different boundary conditions (periodic and open) and tested the effect of the random phase.

While using just open boundary conditions may seem physically more reasonable, our 2.5-D simulations would basically allow infinitely long KH wavelength for the open boundary conditions. In the real magnetosphere the field line curvature (3-D effect) will set a limit to the maximum wavelength of the KH wave and infinitely long waves cannot occur at the magnetopause [*Ma et al.*, 2014a, 2014b]. Therefore, it is useful to study also periodic boundary conditions, where the maximum KH wavelength is restricted to the length of the simulation box (38 R_E). Since the initial perturbation is set on the upstream boundary and we only follow the simulation for 14.5 min, the periodic boundary conditions will not disturb the KH development in the region of interest but just ensure that maximum wavelength cannot exceed 38 R_E.

3. Results

3.1. Evolution of the KHI Due To Single-Mode Seed Fluctuations

Figure 2 illustrates plasma number density and velocity (a), total pressure (b), and perpendicular velocity (with respect to initial shear flow boundary), v_y (c) at $t = 406$ s for a 6.86 mHz mode in the macroscale simulation. The KH wave can be seen at $x \approx -150$ which is evidenced as density, total pressure, and perpendicular velocity perturbation. The rest of the KH wave plots shown in this paper are zoomed in magnifications of this large-scale simulation box. As seen from Figure 4 in *Dimmock and Nykyri* [2013], the MSH velocity typically varies between 0.1 and 0.7 V_{sw} from subsolar point to the dawn-dusk terminator. The velocity shear magnitude at the simulation boundary at $x = -200$ is chosen after the statistically observed velocity downstream from subsolar point and is set to −155 km/s.

Figure 3 shows the growth of the KHI ln(max (δv_y)) as a function of time for $v_1 = 0.065$ and for $v_1 = 0.25$ with $f = [0.5, 1, 2, 3, 4, 8, \text{and} 15] f_{\text{fg}}$. The growth is measured by the maximum amplitude of the normal velocity component (along the extent of the velocity shear layer and starting from one grid point above the initial seed perturbation) on the magnetospheric side of the velocity shear layer close to the initial boundary. The first stage of growth for $t < 25$ s is due to the system response to the initial driving. The second stage is the somewhat flat region, which is clearly observed for high-frequency cases and is due to the growth of very small-scale KH waves which rapidly decay, until the most unstable stage (stage 3) is reached. The fourth and final stage is the saturation. For the third stage (exponential growth) the highest amplitude is first reached for the theoretical fastest growing mode with $f = f_{\text{fg}}$ (red curve) at $t = 210$ s. The nonlinear stage, t_{nl}, for this mode is reached about 90 s sooner for the larger initial perturbation amplitude. For low-amplitude seed, the nonlinear stage KH wave is reached latest for the highest seed frequency, $f = 15 f_{\text{fg}}$ (yellow curve) at $t = 400$ s. Figure 4 shows the time evolution of the KH waves at $t = 197$ s, 348 s, 499 s, and at 652 s in a zoomed box inside the large-scale simulation in $[x = -200, -50]$ to $[y = -15, 15]$ for $v_1 = 0.0625$ for the $f = 15\ f_{\text{fg}} = 102.9$ mHz (a) and $f = 1 f_{\text{fg}} = 6.86$ mHz (b) seed perturbation (see the red and yellow curves in Figure 3). It is clear that the 6.86 mHz seed produces a faster growing and a larger amplitude KH wave than the 102.9 mHz seed. The wavelengths of the observed KH waves measured at $t = 348$ s are approximately $\lambda = 1.7$ and 3.5 R_E for 102.9 mHz mode and 6.86 mHz mode, respectively. These wavelengths are of the same order as the wavelength of the theoretical fastest growing mode, $\lambda \approx (2-4)\pi\Delta = 1.8-3.6 R_E$ using shear layer width, $\Delta = 1800$ km in agreement with *Miura and Pritchett* [1982]. By $t = 652$ s, the low-frequency seed has produced a larger-scale KH structure than the high seed frequency.

3.2. Plasma Transport

Tables 2 and 3 list the times for CASES 1A, 1B, and 1C and 2A, 2B, and 2C, respectively, when the plasma transport starts, t_{m0}, when the maximum plasma transport velocity is reached, t_{mmax}, and the corresponding maximum plasma transport velocity, v_{max}. It can be seen that for the larger-amplitude initial seed fluctuation (CASES 2) plasma transport starts sooner ($t_{m0} = 30 - 180$ s) and also the maximum plasma transport rate is typically reached sooner ($t_{\text{mmax}} = 180-770$ s) than for the smaller amplitude initial seed ($t_{m0} = 120-370$ s and $t_{\text{mmax}} = 440-840$ s for CASES 1).

Nearly for all the seed frequencies the maximum transport velocities are higher for the large-amplitude cases (shown in Table 3) when compared to small-amplitude seeds (shown in Table 2). Exception are the high-frequency ($f \geq 4 f_{\text{fg}}$) cases with open boundary conditions. When comparing the large-amplitude, higher-frequency seed cases ($f > 2 f_{\text{fg}}$) with periodic boundary conditions shown in Table 3 (runs 2A and 2B), the maximum plasma transport rates are fairly similar (within 210–260 m/s).

For higher-resolution periodic boundary conditions (CASES 1B and 2B) the maximum plasma transport velocities are obtained when seed frequency is equal to the theoretical fastest growing mode ($f = f_{\text{fc}}$). Figure 5

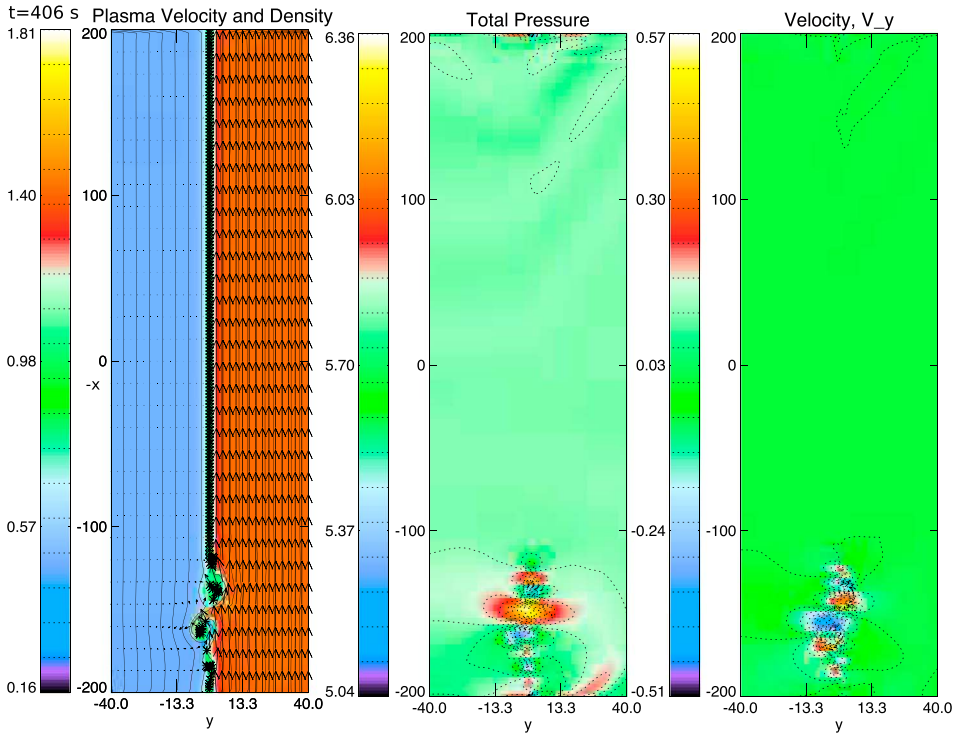

Figure 2. Simulation domain at $t = 406$ s. Vectors present plasma velocity and color code is (left) density, (middle) total pressure, and (right) perpendicular velocity. The black lines are magnetic field lines. The total x range from −200 to 200 is shown. The KH ripples are visible at $y, x = [0, -150]$. Magnetosheath (magnetosphere) is on the right (left), and KH wave is propagating upward.

shows a snapshot of the KH structure at $t = 440$ s of the comparison between the cases with $v_1 = 0.0625$ (a) and $v_1 = 0.25$ (b) and $f = 1f_{fg} = 6.86$ mHz. For the larger-amplitude seed, more magnetosheath material has reconnected by $t = 440$ s, corresponding to plasma entry velocity of $\approx$ 530 m/s. For smaller-amplitude seed, the main vortex is smaller and maximum transport velocity of 480 m/s is reached 400 s later. For lower resolution and periodic boundary conditions (CASES 1A and 2A) the maximum plasma transport velocities of 330 m/s and 880 m/s are obtained when seed frequency is half of the theoretical fastest growing mode ($f = 0.5f_{fc}$). When considering all the cases, the largest transport velocity of $\approx$ 1.1 km/s occurs for the open boundary conditions when the magnetosheath driver frequency is 0.5 f_{fg} and $v_1 = 0.25$.

The plasma transport calculation presented in Tables 2 and 3 utilize 201 plasma fluid elements placed at the magnetopause, whose vector potential value is used to define the original magnetopause boundary using equation (3). To estimate the error in plasma transport calculations, due to possible inaccuracies in boundary determination, we have computed for CASES 1B and 2B the mass transport velocities also using 101 fluid elements. With 101 fluid elements $v_{max} = [280, 470, 130, 120, 80, 100, 150]$ m/s and for the seed frequencies, $f = [0.5, 1, 2, 3, 4, 8, 15]\ f_{fg}$. The error is thus at least about 10–20 m/s for the higher-frequency cases and about 90 m/s for the lowest frequency. For larger-amplitude cases (CASES 2B), with 101 fluid elements $v_{max} = [510, 600, 270, 270, 230, 220, 220]$ m/s and for the seed frequencies, $f = [0.5, 1, 2, 3, 4, 8, 15]\ f_{fg}$, so the error is around 10–20 m/s for higher-frequency ($f \geq 2f_{fg}$) cases and 70 m/s for $f = f_{fg}$. Interestingly, exactly the same value was observed for the lowest-frequency case. When considering the open boundary conditions and the same resolution as for 2B (CASE 2C), the plasma transport rates have significantly increased (doubled) for the lowest-frequency case. This is because for the open boundary conditions and for a large simulation box size perpendicular to initial shear flow layer, there is no limit for the maximum wavelength. The lowest-frequency seed creates a very large vortex size, and associated reconnection leads to more plasma transport.

Perhaps the most striking difference is that for the large-amplitude, high-frequency ($f \geq 8f_{fg}$) seed with open boundary conditions (CASE 2C), the transport rates are significantly lower than for the corresponding low-amplitude seeds. This is because the high-frequency, high-amplitude seed generates a train of short

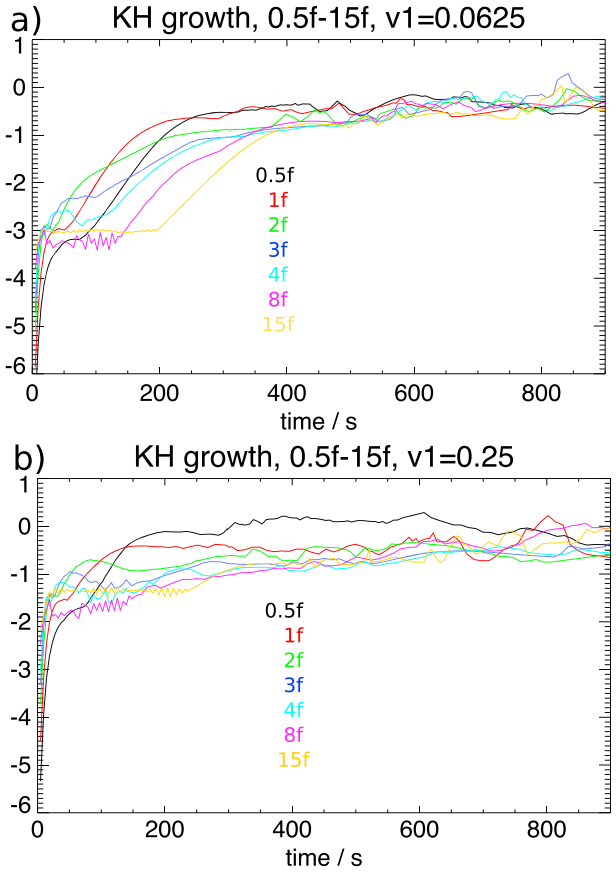

Figure 3. The growth (ln(max(δv_y)) of the KHI for seven different magnetosheath seed frequencies and for two different amplitudes: (a) $v_1 = 0.0625$ and (b) $v_1 = 0.25$. (CASES 1A and 2A).

wavelength waves that grow nonlinearly very quickly and merge back into magnetosheath plasma, resulting in reduced transport when compared to the low-amplitude seed, where these small-scale reconnected magnetic islands move farther away from the original boundary contributing to the net plasma transport. It is also interesting that for the low amplitude, highest seed frequency, and for open boundary conditions, one gets more transport than for the seed frequency equal to the theoretical fastest growing mode f_{fg}. This is because the open boundary conditions create a larger wavelength KH wave, and the continuous driving with the low-amplitude high-frequency seed contributes to the breaking of the large-scale vortex structure. At the magnetopause, the curvature of the magnetic field line localizes the KH unstable region at low latitudes. The kinetic energy associated with KH vortex will be radiated to the high latitudes by the Poynting flux. Scaling analysis and numerical experiment shows that an over slow growing (i.e., an over long wavelength) KH mode cannot occur at the magnetopause [*Ma et al.*, 2014a, 2014b].

3.3. Evolution of the KHI Due To Multimode Seed Fluctuations With the Different Amplitudes Between the Modes (CASE 3)

In the real magnetosheath, the amplitude of the fluctuations is typically larger at low frequencies compared to high frequencies, so it is necessary to study the effect of a more realistic spectra by varying the fluctuation amplitude between the modes. The amplitude of the nth mode is computed as $A_n = v_1/n$, where $v_1 = 0.25$ and the phase is different for each mode. Figure 6 shows that the growth rates of the KHI for multimode seed spectra are fairly similar to each other. Table 4 shows the quantified plasma transport rates for CASE 3 in the same format as in Tables 2 and 3. For $N = 2, 5$, and 10 we have also tested the effect of numerical resolution and periodic versus open boundary conditions (CASES 3A, 3B, and 3C). It is evident that there is less variation of the times when reconnection starts ($t = 80–190$ s) when compared to the single-mode runs ($t = 30–350$ s) (CASES 1 and 2). Also, the maximum plasma transport velocities show less variation and are typically higher for multimode seed spectra ($v_{max} \approx 410–930$ m/s) than for single-mode seed fluctuations ($v_{max} \approx 30–1090$ m/s). The large-scale KH structure of all these multimode cases, where the lowest frequency

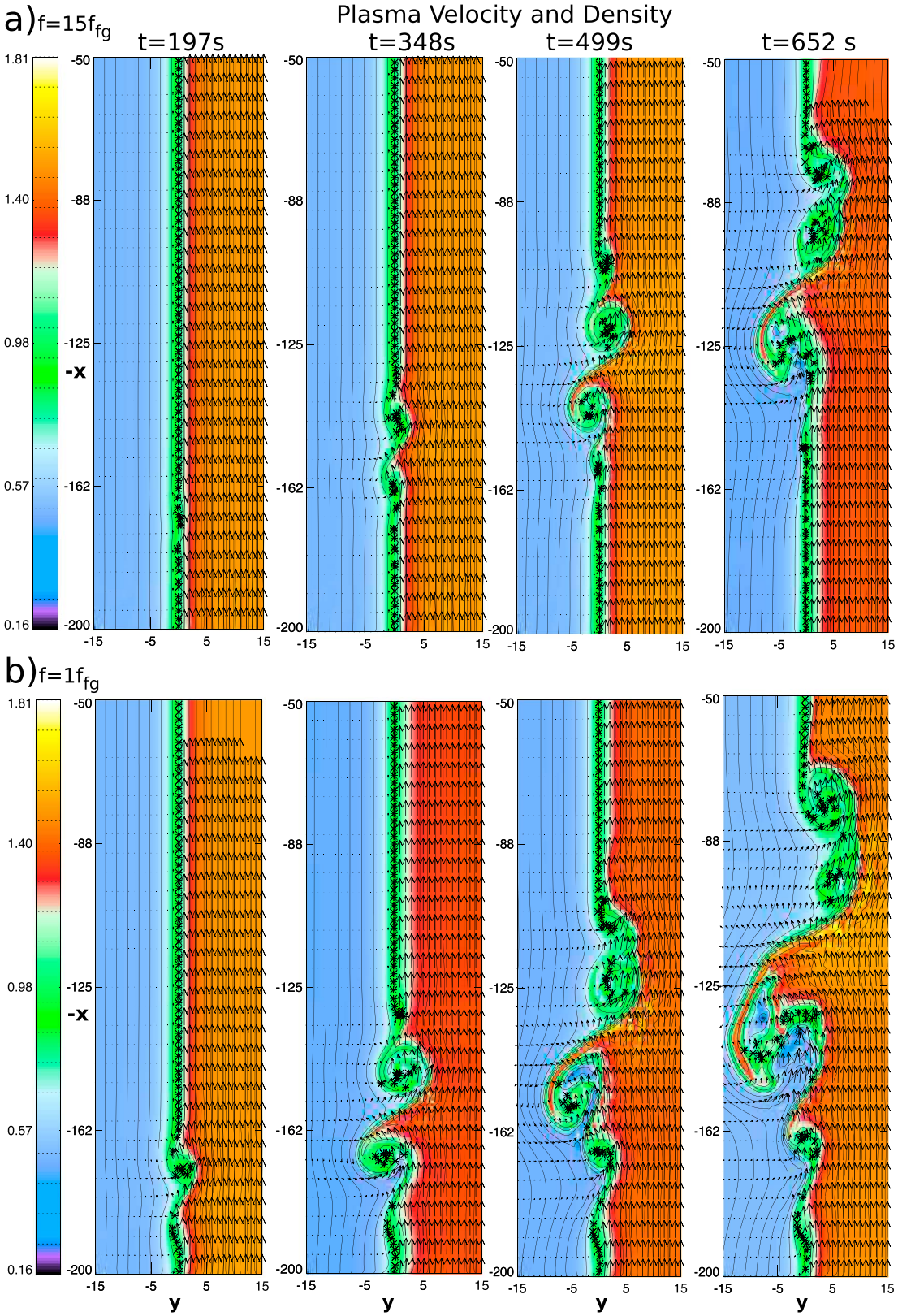

Figure 4. Snapshots during four different times of the KH dynamics in a smaller subdomain (x range = [−200, −50], y range = [−15, 15]) for (a) low-frequency ($f = 1\ f_{fg}$) and (b) high-frequency ($f = 15\ f_{fg}$) seeds for $v_1 = 0.0625$ (CASE 1A). Background color is plasma density, and arrows are velocity vectors. The KH growth for these cases is depicted in red and yellow lines in Figure 3a.

Table 2. Plasma Transport Results for Runs Shown in Figure 3 (CASE 1A) Corresponding to the Single-Mode Seed Frequency Cases With $v_1 = 0.0625$[a]

CASE f	1A, 1B, 1C t_{m0} (s)	1A, 1B, 1C t_{mmax} (s)	1A, 1B, 1C v_{max} (m/s)
$0.5f_{fg}$	350, 340, 200	670, 740, 600	330, 190, 400
f_{fg}	200, 210, 230	440, 840, 620	250, 480, 370
$2f_{fg}$	240, 260, 170	800, 440, 440	110, 120, 270
$3f_{fg}$	170, 190, 190	660, 470, 640	30, 100, 350
$4f_{fg}$	200, 140, 120	650, 780, 780	60, 70, 350
$8f_{fg}$	260, 200, 270	540, 590, 540	50, 90, 420
$15f_{fg}$	460, 200, 310	600, 550, 560	160, 140, 750

[a]Here f_{fg} corresponds to the frequency of the theoretical fastest growing mode, t_{m0} to a time when mass transport starts, t_{mmax} to a time when maximum plasma transport is reached, and v_{max} to a maximum mass transport velocity. The second value is for the case with double the resolution along the shear flow (x) direction (CASE 1B). The third value is for the open boundary condition in x_{max} and with the double resolution along x (CASE 1C).

present is $f = 0.5f_g$, is very similar to the single-mode case with $v_1 = 0.25$ and $f = 0.5f_{fg}$. To check whether this is because the lowest frequency has the highest amplitude and therefore dominates the large-scale KH structure, we also created multimode runs with $N = 2$–10 and kept the same amplitude $v_1 = 0.0625$ for each mode. Even in this case, the large-scale structure was similar as for the single-mode seed with the lowest frequency. When comparing cases 3A, 3B, and 3C for the $N = 2$ case which has both the lowest and the highest frequencies, most transport ($v_{max} = 930$ m/s) occurs for the open boundary conditions. This is consistent and can be understood with the single-mode cases: the highest mass transport velocity of 1090 m/s occurred for open boundary conditions, highest amplitude, and lowest-frequency seed, while the highest-frequency seed yielded the largest transport velocities of 750 m/s for the low-amplitude case. For the $N = 2$ case both of these frequencies are present with $f = 0.5f_{fg}$ and $f = 15f_{fg}$ having the amplitudes of 0.25 and 0.125, respectively. This seed frequency combination creates a large wavelength KH wave where the high-frequency seed spectrum produces additional transport.

A large transport velocity of 920 m/s occurs also for the low-resolution, periodic boundary conditions with $N = 5$, which is nearly the same ($v_{max} = 880$ m/s) as for the single-mode case for $f = 0.5f_{fg}$ and $v_1 = 0.25$ (CASE 2A), so clearly there are other frequency/wavelength combinations that yield optimal transport. However, when the resolution for this case is increased (CASE 3B) the transport velocity is reduced to 640 m/s,

Table 3. Plasma Transport Results for Runs Shown in Figure 3 (CASE 2A) Corresponding to a Single-Mode Case With $v_1 = 0.25$

CASE f	2A, 2B, 2C t_{m0} (s)	2A, 2B, 2C t_{mmax} (s)	2A, 2B, 2C v_{max} (m/s)
$0.5f_{fg}$	180,180,120	600, 530, 590	880, 510, 1090
f_{fg}	110, 100,120	420, 440, 450	650, 530, 510
$2f_{fg}$	70, 60, 70	260, 230, 510	250, 290, 590
$3f_{fg}$	100, 90, 50	380, 500, 760	210, 260, 360
$4f_{fg}$	70, 50, 70	180, 770, 410	260, 240, 300
$8f_{fg}$	50, 40, 60	340, 550, 380	230, 210, 150
$15f_{fg}$	80, 30, 30	430, 500, 690	260, 240, 220

[a]The second value refers to the case with double the resolution along the shear flow (x) direction (CASE 2B). The third value is for the open boundary condition in x_{max} and with the double resolution along x (CASE 2C).

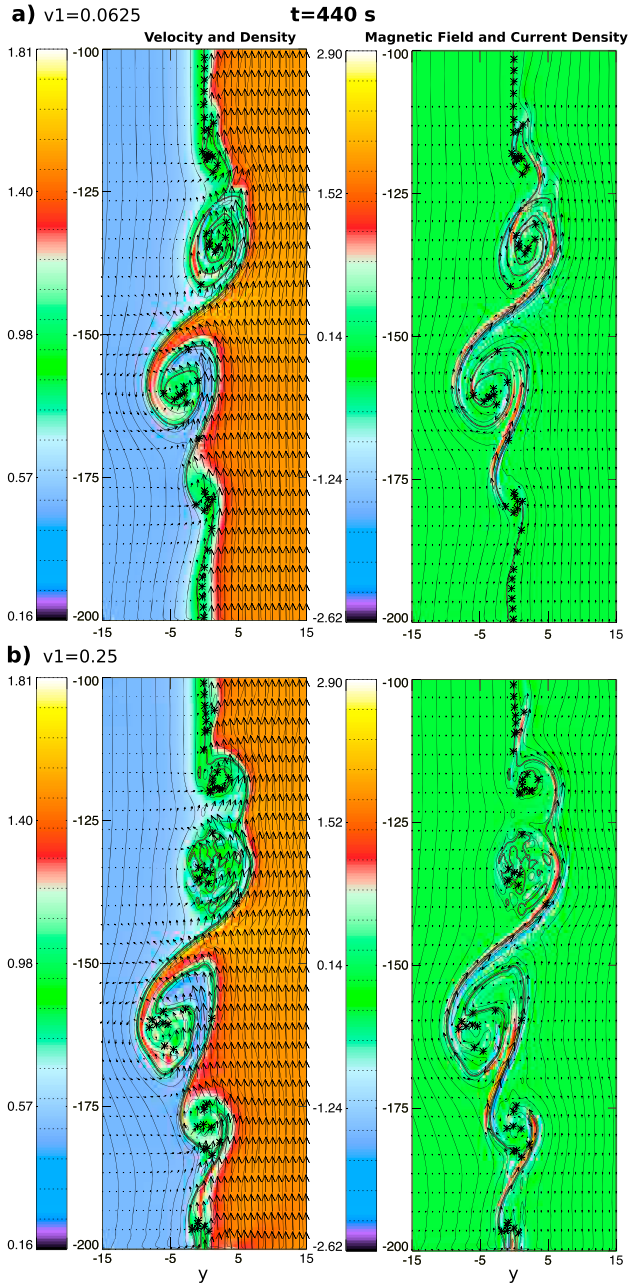

Figure 5. Comparison of the structure of the KH wave at $t = 440$ s for (a) smaller- and (b) larger-amplitude seed perturbations for $f = 1f_{fg}$ (CASES 1B and 2B). The left column depicts the plasma density and velocity, and right column shows the current density and magnetic field. The black solid lines are the magnetic field lines.

because the various small-amplitude high-frequency modes are better resolved during the early times of simulation, which leads to broader boundary layer and suppression of the intermediate wavelength modes, thus resulting in reduced transport (see Appendix B for further details).

3.4. Impact of Random Phase

In the single-mode simulations (CASES 1 and 2), the initial random phase was $\phi = 6.27$ rad. Table 5 shows results of the maximum mass entry velocities for CASE 1A ($v_1 = 0.0625$) when considering three additional initial phases, all separated by $\pi/2$. For the single-mode fluctuations the initial random phase seems to make a difference. For example, for $f = f_{fg}$, the highest mass entry velocity of 360 m/s is obtained for $\phi = 4.70$ rad, and the lowest velocity of 40 m/s occurs for $\phi = 1.56$ rad. For $f = 8f_{fg}$, the maximum velocity of 330 m/s occurs

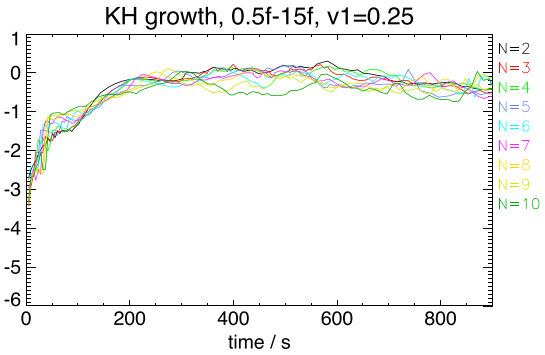

Figure 6. Comparison of the the KH growth (same format as in Figure 3) when different amounts of modes (2–10) are placed with equifrequency intervals at the continuum Pc5–Pc2 range with different amplitudes in each frequency.

also for $\phi = 4.70$, whereas the lowest velocity of 50 m/s occurs for $\phi = 6.27$ rad. The discrepancy is of 1 order of a magnitude.

When calculating the average of the maximum mass entry velocity for these different phases at each frequency, the highest average mass entry velocity of 200 m/s is obtained for the theoretical fastest growing mode ($f = f_{fg}$) and smallest average velocity of 60 m/s for $f = 3f_{fg}$. When calculating the average over all frequencies for each phase, the highest (lowest) average velocity of 180 m/s (70 m/s) occurs for $\phi = 4.70$ rad ($\phi = 1.56$ rad).

To better understand the physical reason for these differences, we have compared the seed velocity perturbation, δv_y, time series for these 28 cases and compared the time integral of the velocity perturbation experimentally for different time periods. We found that for each frequency, the maximum mass entry velocity occurred for the phase which produced the largest positive value of the integral, $\int_0^{145s} \delta v_y \, dt$. The time 145 s, which was experimentally found, roughly corresponds to the time by which the shortest wavelengths have saturated and longer wavelengths are growing or are about to grow. This comparison is depicted in Figure 7, which clearly shows that the maximum positive area underneath the curve occurs for $f = 0.5f_{fg}$ with $\phi = 6.27$ rad (black curve) and for $f = 1f_{fg}$ with $\phi = 4.7$ rad (red curve).

To test the effect of a different initial phase on the multimode seed, we changed the phase of the lowest-frequency and highest-amplitude mode from $\phi = 6.27$ rad to $\phi = 1.56$ rad for the $N = 5$ case, which reduced the maximum mass entry velocity from 920 m/s to 680 m/s. The other phases of the higher-frequency modes were kept unchanged. So the initial phases for $N = 5$ case depicted in Table 4 were changed from 6.27, 3.56, 6.07, 4.70, and 2.31 rad to 1.56, 3.56, 6.07, 4.70, and 2.31 rad. Figure 8 shows the comparison between

Table 4. Effect of the Multimode Seed on the Plasma Transport (CASE 3)[a]

N	t_{m0} (s)	t_{mmax} (s)	v_{max}
CASE	3A, 3B, 3C	3A, 3B, 3C	3A, 3B, 3C
2	180, 190, 150	610, 510, 590	640, 410, 930
3	180, ***, ***	630, ***, ***	520, ***, ***
4	180, ***, ***	560, ***, ***	690, ***, ***
5	180, 80, 120	540, 600, 640	920, 640, 570
6	180, ***, ***	590, ***, ***	800, ***, ***
7	180, ***, ***	500, *** , ***	740, ***, ***
8	190, ***, ***	520, ***, ***	750, ***, ***
9	190, ***, ***	490, ***, ***	770,***, ***
10	170, 110, 140	510, 600, 330	830, 570, 790

[a]Number of modes at $(0.5–15)f_{fg}$ range, t_{m0}, t_{mmax}, and v_{max}. Each mode (i) has a different amplitude, $v_1 = 0.25/i$, and different random phase, ϕ. For $N = 2, 5$, and 10 we have also tested the effect of two different resolutions and open boundary conditions (CASES 3A, 3B, and 3C.). Asterisks mark cases for which no simulation was performed.

Table 5. CASE4[a]

f	ϕ = 1.56 rad	ϕ = 3.13 rad	ϕ = 4.70 rad	ϕ = 6.27 rad	V_{ave}
$0.5f_{fg}$	50	50	30	330	120
f_{fg}	40	160	360	250	200
$2f_{fg}$	60	40	110	110	80
$3f_{fg}$	40	50	100	30	60
$4f_{fg}$	40	50	100	60	60
$8f_{fg}$	130	200	330	50	180
$15f_{fg}$	160	70	240	160	160
V_{ave}	70	90	180	140	130

[a]The maximum mass entry velocities (in m/s) for different initial phases, ϕ, for CASE 1A (v_1 = 0.0625), average mass entry velocity for each frequency (last column), and for each phase (last row).

these two cases depicting the seed velocity perturbation, δv_y, time series. It is clear from the graph that the case with ϕ_{N_1} = 6.27 rad has a larger positive area when compared to case with ϕ_{N_1} = 1.56 rad. This is also verified by evaluating the integral $\int_0^{145s} \delta v_y \, dt$. This 240 m/s difference in mass entry velocity due to the highest-amplitude mode phase variation is 30% of the average v_{max} = 800 m/s.

The physical meaning of $\int_0^{145s} \delta v_y \, dt$ may be interpreted as the average indentation length scale of the magnetopause boundary during the growth of the KHI, with the larger values resulting in larger vortex sizes and more transport. When we evaluated this integral for the nine cases with N = 2–10, the values of this integral

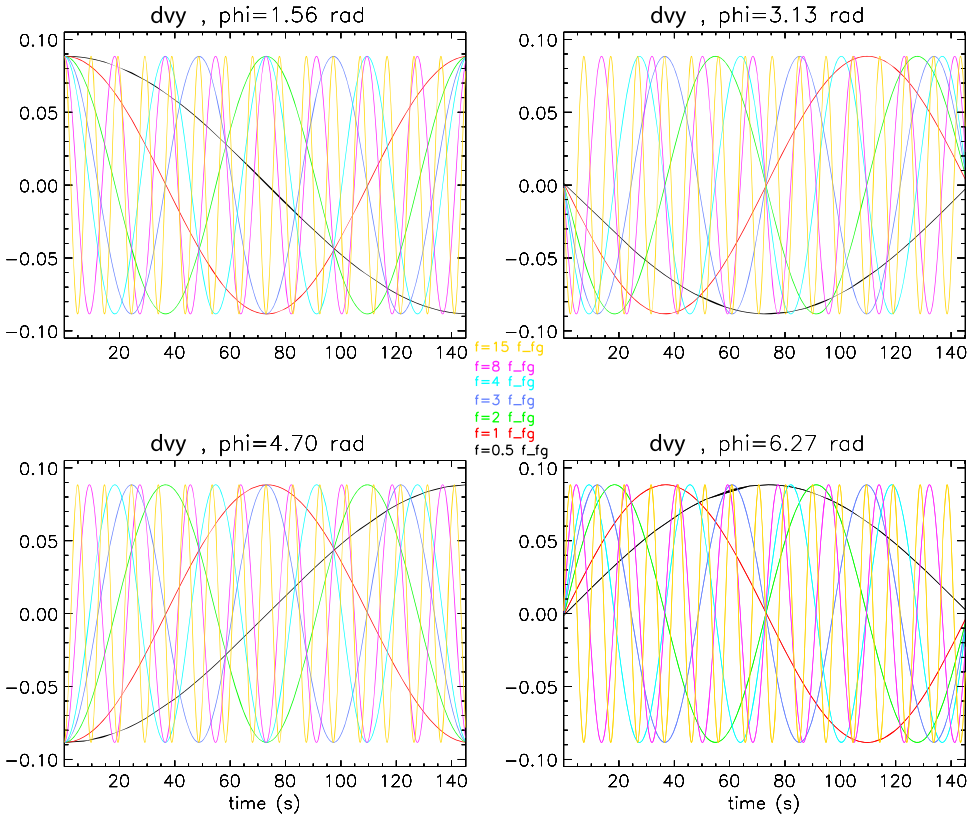

Figure 7. The velocity perturbation, δv_y, as a function of time for seven different frequencies, f = (0.5, 1, 2, 3, 4, 8, 15) f_{fg} (depicted by black, red, green, blue, aqua, magenta, and yellow lines, respectively) at four different initial phases: ϕ = 1.56, ϕ = 3.13, ϕ = 4.70, and ϕ = 6.27 rad.

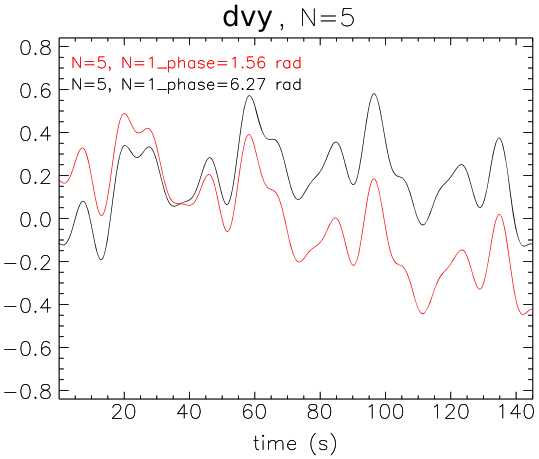

Figure 8. The velocity perturbation, δv_y, as a function of time for the case where five modes ($N = 5$) are in Pc2–Pc5 range. The spectrum is identical except that the phase, ϕ, of the first, largest amplitude is changed. The black line depicts the seed spectrum for $\phi_{N_1} = 6.27$ rad, and the red line depicts the seed spectrum with $\phi_{N_1} = 1.56$ rad.

were almost identical (see the corresponding velocity perturbation time series in Figure 9). For all these nine cases the phase for the lowest-frequency, highest-amplitude mode was the same. The largest mass transport velocity of 920 m/s occurred for $N = 5$ case at $t = 540$ s, whereas the lowest velocity of 520 m/s occurred for $N = 3$ case at $t = 630$ s. The variations of the seed spectrum frequencies seem to alter the large-scale vortex structure and hence have some effect on the net plasma transport.

These results suggest that there is an optimal time with respect to KH growth for a given set of plasma parameters and shear layer properties when seed spectrum properties have the strongest impact on the large-scale evolution and plasma transport associated with the KHI. Because in the real system, a case where only a single mode is present is singular, the phase variation study for the multimode run ($N = 5$) is more meaningful. Note that only the phase of the lowest-frequency, highest-amplitude mode was changed, and remaining phases were kept the same. This type of extreme variation probably never happens in the real system, but typically, all the initial phases are different. This 30% variation of v_{max} for $N = 5$ case due to phase, ϕ_1, change is therefore probably an extreme difference and is of the order of variation of mass transport velocities for cases when the number of modes is varied between 2 and 10 (see Table 4). So while the phase variation produces some differences for the results, we do not think that the initial phase is a very important factor for the real system as long as there are many modes in the system with different initial phases.

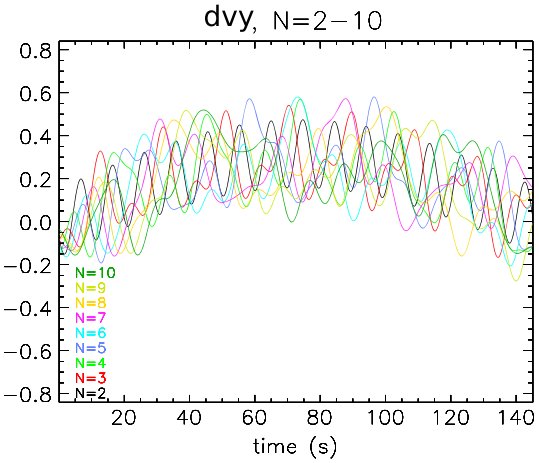

Figure 9. The velocity perturbation, δv_y, as a function of time for the nine cases ($N = 2$–10) in Pc2–Pc5 frequency range.

4. Conclusions

In the present paper we have studied the effect of the frequency, amplitude, and number of modes of the magnetosheath velocity fluctuations on the growth of the Kelvin-Helmholtz instability (KHI) and associated plasma transport. Initial plasma and field conditions for the simulations were taken based on statistical maps using 7 years of THEMIS measurements in the vicinity of the dayside magnetopause during northward IMF. For each run, all the plasma parameters and field configuration are kept the same, the only difference being the structure of the magnetosheath seed fluctuation spectrum. The main findings of the study are as follows.

Single-Mode Seed Analysis:

1. For larger-amplitude seed, KHI reaches the nonlinear stage sooner, and plasma transport starts earlier than for the smaller-amplitude seed.
2. The maximum plasma transport rate is typically reached sooner, and maximum mass transport velocities are typically higher for higher-amplitude seed. Exception are the cases with high seed frequencies ($f \geq 4f_{fg}$) for open boundary conditions due to a merging of small magnetic islands back to the magnetosheath.
3. The KH wave first reaches the largest amplitude when seed frequency is equal to the theoretical fastest growing mode.
4. For periodic boundary conditions, and for small-amplitude seed, the largest transport velocities occur when driver frequency is equal to the frequency of the theoretical fastest growing mode.
5. Open boundary conditions along shear flow create a larger KH wave when compared to periodic boundary conditions and double the mass transport for the lowest-frequency case. The largest transport velocity of 1.1 km/s is obtained for a large-amplitude seed with the seed frequency half of the theoretical fastest growing mode. This is of the same order of magnitude as in the study by *Nykyri and Otto* [2001], which used a larger velocity shear consistent with the Geotail observations of the KHI [*Fairfield et al.*, 2000; *Otto and Fairfield*, 2000] which occurred farther downstream along the flank magnetopause.
6. For large-amplitude, high-frequency seeds ($f \geq 3f_{fg}$), the transport velocities are fairly similar (210–260 m/s) and the variation is of the order of error bars for the periodic boundary conditions.
7. The combination of the phase and frequency of the seed perturbation seems to have effect on mass transport velocities produced by the KHI: the maximum transport velocities for each frequency correlate with the largest positive value of the following integral: $\int_0^{145s} \delta v_y \, dt$. Here the time 145 s was experimentally found and roughly corresponds to the time when shorter wavelength modes have saturated and dominant mode is growing or is about to grow.

Comparison Between Multimode and Single-Mode Seeds:

8. When the seed spectrum consists of 2–10 modes in Pc2–Pc5 range with different amplitudes for each mode (and with $v_1 = 0.25$ for the highest-amplitude mode), the maximum plasma transport velocities are of the order 0.5–1 km/s and higher than the corresponding, high-amplitude single-mode high-frequency cases. This is probably because the multimode seed spectrum contains more energy than the single-mode seed.
9. The phase of the largest-amplitude, lowest-frequency mode in multimode spectrum affects the plasma transport rate produced by the KHI. The case for which the integral $\int_0^{145s} \delta v_y \, dt$ is larger during the exponential growth of the dominant KH mode produces more plasma transport.

5. Discussion

To assess which of these resolutions and boundary conditions are most appropriate when comparing to the real system, one needs to consider the geometry of the magnetosphere. The real magnetosphere has field line curvature, which can stabilize KHI. Therefore, the open boundary conditions which basically allow infinitely long wavelength (and larger than realistic amplitude of the KH wave) may not give the best presentation of the real system. Furthermore, the simulations should have adequate numerical resolution to resolve the small-scale structures resulting from high-frequency seeds. We therefore think that from the presented cases, CASES 1B, 2B, and 3B are probably most meaningful and are used in the following discussion.

These results suggest that the fluctuation properties of the dayside magnetosheath have impact on the growth of the KHI and when reconnection starts. The most plasma transport occurs for the multimode seeds ($v_{max} = 420–640$ m/s) and for the large-amplitude seed with the frequency equal to the theoretical frequency of the fastest growing KH mode f_{fg}($v_{max} = 530–600$ m/s), which corresponds to Pc5 frequency range. The transport velocities of ≈ 0.6 km/s correspond to the diffusion coefficient of $\sim 1.1 \times 10^9$ m^2/s when assuming

a shear layer thickness of 1800 km. These results are slightly smaller than the corresponding plasma transport velocities of 1.7–2.3 km/s for the 5° tilt case in *Nykyri and Otto* [2001]. This is not surprising because the initial conditions for the simulations in the present study correspond to the typical dayside plasma conditions with a modest shear flow of 155 km/s. The simulations in *Nykyri and Otto* [2001] were created after Geotail observations at $x_{GSM} \approx -10\ R_E$, corresponding to a wave source region at the dawn-dusk terminator where the shear flow typically is comparable to the solar wind speed and was set to 315 km/s.

The typical timescale for low-amplitude, single-mode seed perturbation to reach maximum plasma transport due reconnection in KH vortices ranged from ~400 s to 800 s and for high-amplitude seed from ~ 200 s to 770 s. For the multimode seed, which is a more realistic presentation of a typical magnetosheath spectrum, the maximum transport velocity is reached within 500–600 s. During this time, the KH wave spectrum has developed large, nonlinear vortices and moved from the source region at the dayside a distance of 7–10 R_E, which suggests that significant boundary layer generation via reconnection in KH vortices becomes possible in the vicinity or slightly downstream of the dawn-dusk terminator for strongly northward IMF.

Based on the present simulations, the amplitude of the excited KH waves and resulting vortex size decreases for the higher-frequency seed spectrum. This may suggest that the magnetosphere-ionosphere coupling is enhanced for the lower-frequency magnetosheath seed perturbations due to generation of field-aligned currents which become stronger as a function of KH vortex size. Also, the reconnected material can pitch angle scatter into the ionosphere thereby affecting ionospheric conductivity, which may have consequences for the large-scale reorganization of the magnetosphere-ionosphere system.

These initial findings of the effect of the theoretical seed spectra on the KHI motivate our future work to determine the statistical spectra of magnetosheath velocity fluctuations as a function of upstream solar wind and IMF conditions. The limitations of the present work are the finite and two-dimensional simulation domain, which limits the study of the evolution of the system up to 14.5 min. It is possible that in an open system and after time $>>$ 14.5 min, the main island gets reconnected significantly farther downstream regardless of the detailed properties of the initial seed spectrum. However, we believe that the present results are valid for describing the impact of magnetosheath seed fluctuation spectrum on the KHI-driven plasma transport at the dayside magnetopause ($t < 14.5$ min). Large-scale, high-resolution 3-D simulations of the KHI dynamics driven by a realistic magnetosheath spectrum constructed after observed statistical spectra would be needed to fully understand the effects of seed fluctuation properties on KHI.

The field line resonances can be produced by the KHI [*Mann*, 1997]. These magnetospheric ULF waves which can resonantly interact, and energize radiation belt particles [*Elkington et al.*, 1999], are mostly observed on the dawn sector which is statistically downstream of the quasi-parallel shock. The foreshock-driven large-amplitude fluctuations may penetrate into the magnetosheath and drive KHI more effectively in the dawn flank. Recent statistical studies have indeed found more Pc3–Pc5 range fluctuations at the dawn sector magnetopause consistent with the frequency range of fastest growing KH mode [*Nykyri and Dimmock*, 2016; *Dimmock et al.*, 2016].

To conclude, we propose that the solar wind and foreshock fluctuations can alter the fluctuation state of the magnetosheath and, hence, transport of plasma and heating. When the larger-amplitude (≈37 km/s) low-frequency (2–5 min) velocity fluctuations are present in the dayside magnetosheath, the KHI can reach nonlinear state faster and produce more plasma transport through the dayside magnetopause. Our statistical THEMIS study indicated that the larger-amplitude velocity perturbations are present for the higher solar wind speeds. Therefore, during faster solar wind speed there is a combined effect from more intense sheath perturbations and a higher velocity shear. The KH waves can in turn generate ion-scale kinetic Alfvén and magnetosonic waves, which can produce additional plasma transport and heating [*Chaston et al.*, 2007; *Moore et al.*, 2016]. The asymmetric growth of the KHI, favoring the dawnside flank, may also help explain the dawn-favored plasma sheet asymmetry of the cold-component ions.

The results we found are also highly interesting because the large-scale solar wind drivers of magnetospheric disturbances and radiation belt electron flux variation have different fluctuation patterns. Sheath regions driven by coronal mass ejections (CME) and slow-fast stream interaction regions have distinctly more turbulent structure when compared to the flux rope part of the CME [*Kilpua et al.*, 2013; *Hietala et al.*, 2014; *Kilpua et al.*, 2015]. Some of the fluctuations in CME sheath regions may be generated by the KHI [*Foullon et al.*, 2011, 2013; *Nykyri and Foullon*, 2013]. In addition, *Nemecek et al.* [2002] found that the level of magnetosheath ion

flux fluctuations increases from the bow shock toward the magnetopause. More detailed work, regarding the characteristic velocity and density fluctuations in different solar wind structures, and how they affect the magnetosheath properties and KHI at the magnetopause, is left for future studies. This is also an important aspect in understanding how different solar wind conditions excite ULF waves through KH waves and their subsequent effects on radiation belt dynamics.

Appendix A

In order to produce a map of magnetosheath velocity fluctuations in Figure 1, THEMIS probe locations between 2008 and 2015 from the geocentric solar ecliptic (GSE) frame are transformed into the magnetosheath interplanetary medium (MIPM) reference frame [*Verigin et al.*, 2006] in order to avoid the effects associated with planetary aberration and motion of the magnetosheath boundaries due to changing solar wind conditions. In MIPM frame the x axis is along to the mean solar wind flow direction, the y axis is a function of IMF vector, and z axis completes the coordinate system. In MIPM frame, the dawn (dusk) flank is downstream of quasi-parallel (perpendicular) shock. Each 3 min THEMIS probe position is normalized between the magnetosheath model boundaries $F_{\mathrm{MIPM}} = 0$ [magnetopause] $\rightarrow 1$ [bow shock]. The position of the magnetopause [*Shue et al.*, 1998] and bow shock [*Verigin et al.*, 2001] models is evaluated based on 20 min averages of the OMNI data. For each 3 min window, the statistical properties of velocity (V) fluctuations are computed and then recorded into a statistical database. Velocity measurements within each window are rotated to a mean flow-aligned (MFA) coordinate system ($\mathbf{V}_{\mathrm{MFA}} = [\hat{V}_{\parallel}, \hat{V}_{\perp(1)}, \hat{V}_{\perp(2)}]$) based on the background flow direction ($\hat{V}_0$) over each 3 min period in a same way as in *Nykyri and Dimmock* [2016]. Perpendicular velocity fluctuations are then evaluated as $V_{\perp} = \sqrt{\left(\mathbf{V}\cdot\hat{V}_{\perp 1}\right)^2 + \left(\mathbf{V}\cdot\hat{V}_{\perp 2}\right)^2}$, where $\hat{V}_{\parallel} = [\bar{V}_x, \bar{V}_y, \bar{V}_z]/\sqrt{\bar{V}_x^2 + \bar{V}_y^2 + \bar{V}_z^2}$, $\hat{V}_{\perp 1} = \hat{V}_{\parallel} \times \hat{R}$, and $\hat{V}_{\perp 2} = \hat{V}_{\parallel} \times \hat{V}_{\perp 1}$. The $V_{x,y,z}$ and $\hat{R}$ correspond to the velocity flow directions and probe location in the GSE frame, respectively.

Statistical maps of $V_{\perp}$ are then created at each location in the MIPM frame equatorial plane. The absolute value of the range (maximum-minimum) of $V_{\perp}$ measurements during each 3 min THEMIS interval is recorded and is placed inside a $0.5 \times 0.5\ R_E$ bin based on its $[x_{\mathrm{MIPM}}, y_{\mathrm{MIPM}}]$ coordinate. A mean average of the ranges of $V_{\perp}$ is then computed inside each bin which is then plotted to produce statistical maps. The complete database was filtered with respect to upstream solar wind conditions to provide additional sub–data sets for slow solar wind ($V_{\mathrm{sw}} < 400$ km/s) and fast solar wind ($V_{\mathrm{sw}} > 400$ km/s). We have used this statistical frame in several publications [*Dimmock and Nykyri*, 2013; *Dimmock et al.*, 2014, 2015; *Nykyri and Dimmock*, 2016] and refer the reader to find more detailed description of this methodology there.

Appendix B

Figure B1 shows comparison of the KHI dynamics for two of the lowest and the highest seed frequency for different boundary conditions (BCs) and numerical resolutions (see caption for more details). Note that for the periodic BCs, and for the high frequency seed, the reconnection in the current layer of the thin-filamented magnetic island is only resolved by $t = 562$ s for the high-resolution case (1B). For the lower-resolution case this island gets reconnected by $t = 600$ s. It is also evident that the open BCs (column 1C) create larger KH structure when compared to the periodic BCs (1A and 1B).

Figure B2 shows comparison of the KHI dynamics for the multimode runs (CASE 3A) and with different amplitudes for each mode (see caption for more details). It is evident that while the large-scale structure is fairly similar for all cases and is dominated by the lowest-frequency mode, $f = 0.5\, f_{\mathrm{fg}}$, the fine structure and reconnection dynamics are different due to the higher-frequency seeds. Note that for $N = 10$ case, the main magnetic island was reconnected already at $t = 510$ s, but by $t = 562$ s it has moved back to the magnetosheath.

Figure B3 shows comparison of the KHI dynamics for the multimode runs, $N = 2, 5, 10$ for CASES 3A, 3B, and 3C and with different amplitudes for each mode (see caption for more details). It is evident that when comparing CASES 3A and 3B, the numerical resolution and seed frequency spectrum all affect where and when reconnection happens first. When the high-frequency seeds are well resolved (3B), it results in shorter-scale

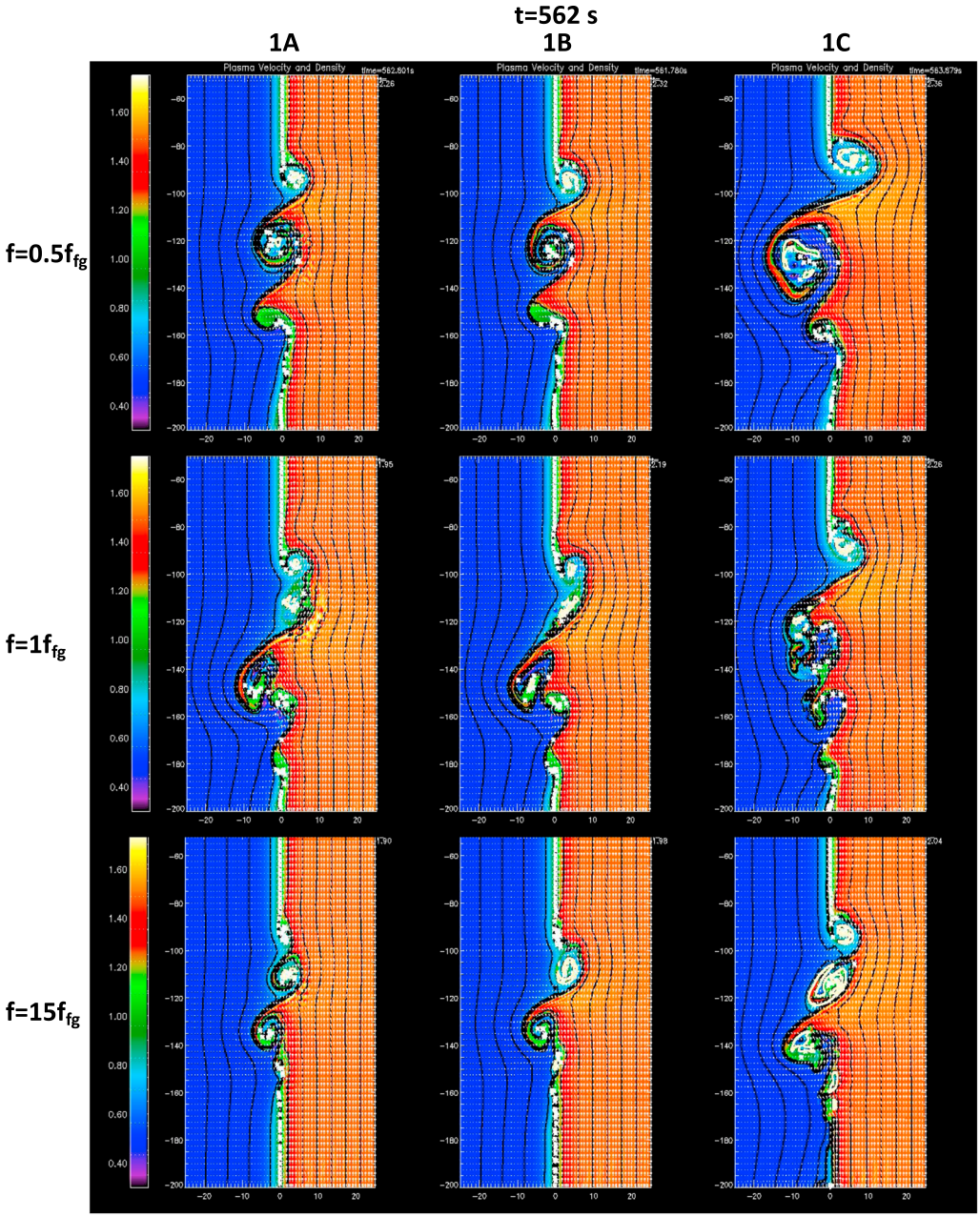

Figure B1. Comparison of the KHI dynamics at $t = 562$ s for (top row) $f = 0.5\ f_{fg}$, (middle row) $f = 1 f_{fg}$, and (bottom row) $f = 15 f_{fg}$ for periodic (1A and 1B) and open (1C) boundary conditions. The 1B and 1C show the high-resolution cases. Background color is the plasma density, black lines are magnetic field, and white arrows are plasma velocity vectors. The white asterisks are fluid elements that are used for boundary calculation. The white thick line illustrates all the closed contours of magnetic vector potential. The closed contours that enclose higher (than surroundings) plasma density are included in the plasma entry (entry from magnetosheath into magnetosphere) calculation. The low-density magnetospheric plasma that is lost into the magnetosheath is excluded from plasma entry calculation.

structures at the very early stage of the simulation, which generates a broader shear layer, thus slowing the growth of intermediate and longer wavelength modes. In lower-resolution run (3A), by $t = 562$ s the three main KH vortices have moved slightly farther downstream when compared to the higher-resolution case (3B) and reconnection of the main island has already happened for $N = 2$ and $N = 5$ cases (for $N = 10$ it happened already at $t = 510$ s and reconnected island has already merged back to the magnetosheath). This is probably

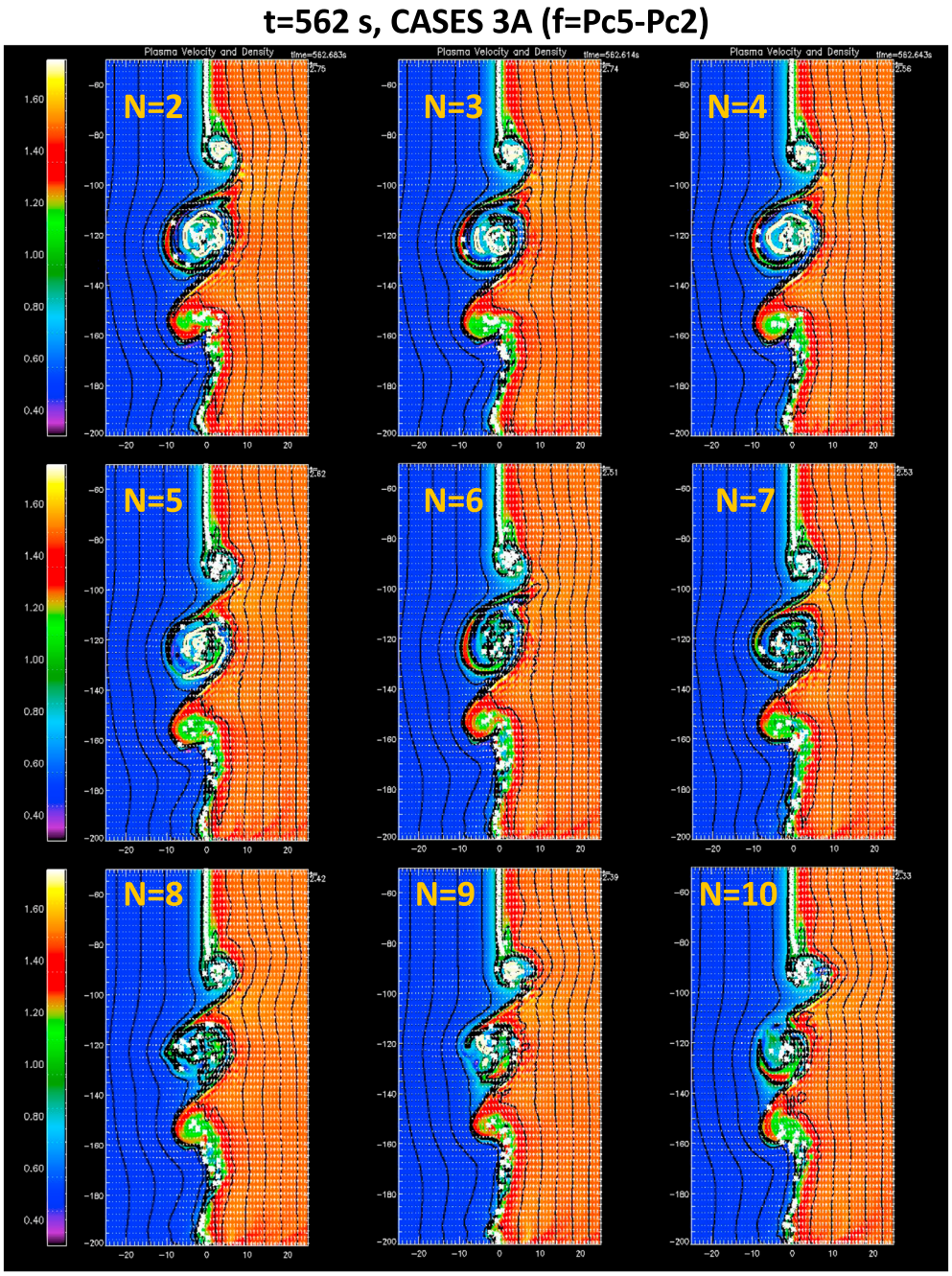

Figure B2. Comparison of the KHI dynamics at $t = 562$ s for multimode runs, $N = 2–10$ (CASE 3A). Each subplot is in the same format as in Figure B1.

because the growth of the intermediate and longer wavelength modes was not disrupted by the dynamics and diffusive boundary layer generated by the higher-frequency seeds. On the other hand, only for the high-resolution cases with $N = 5$ and $N = 10$, the filamentary current layer of the smallest vortex located farthest downstream has been resolved allowing for reconnection to occur. It is also clear that for high-resolution run with $N = 10$, a large region of low-density magnetospheric material is captured into the magnetosheath by $t = 592$ s. This is classified as magnetospheric mass loss into the magnetosheath and is excluded from mass entry calculations. Finally, the open BCs (column 3C) create larger KH structure when compared to the periodic BCs (3A and 3B).

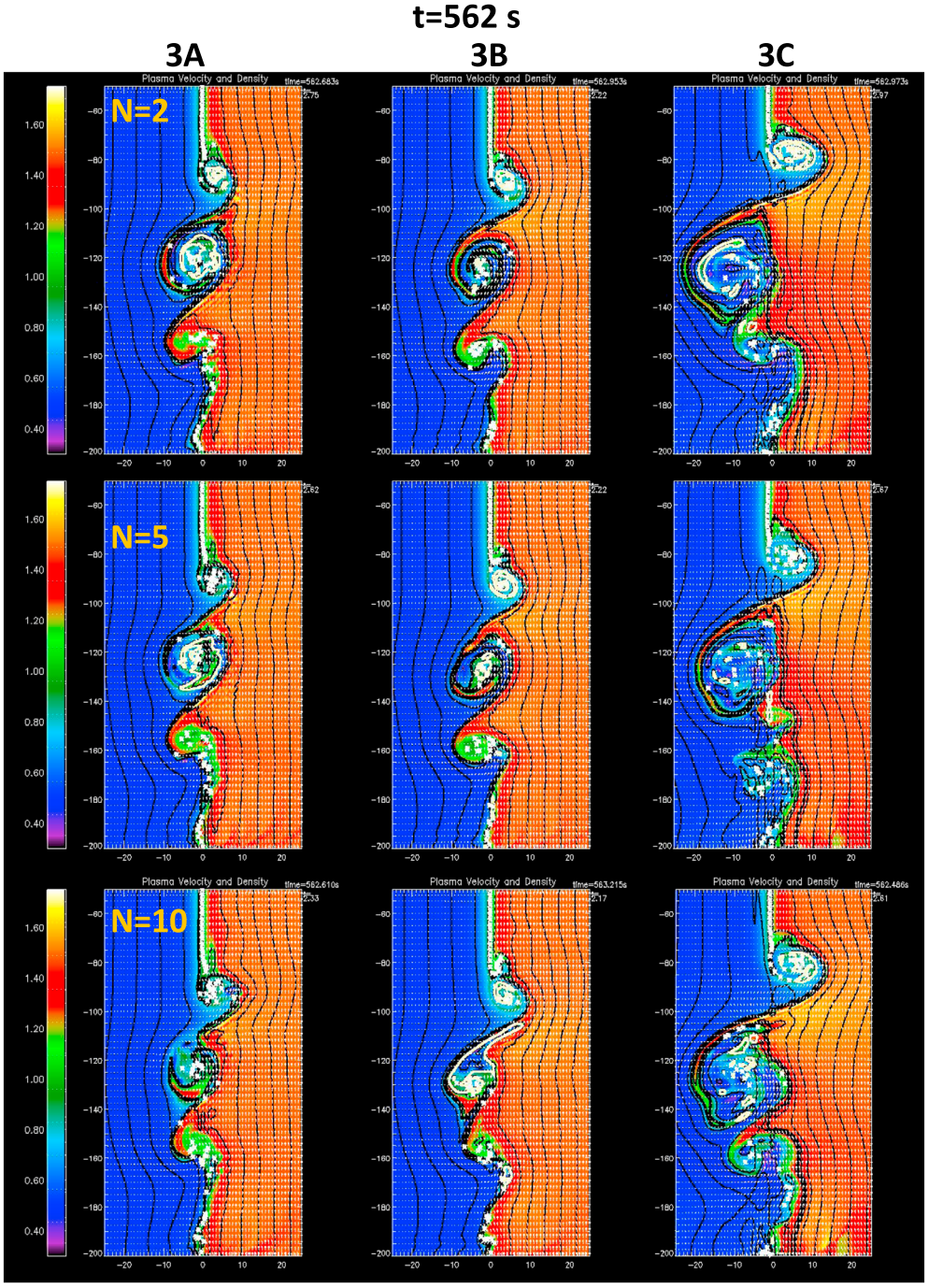

Figure B3. Comparison of the KHI dynamics at $t = 562$ s for multimode runs, $N = 2, 5, 10$ for different BCs and numerical resolutions (CASES 3A, 3B, and 3C). Each subplot is in the same format as in Figure B1.

Acknowledgments
K.N. thanks T. I. Pulkkinen for supporting her visit to Aalto University, Finland, during K.N.'s sabbatical leave from ERAU. K.N. thanks A. Streltsov for comments and E. Kilpua for helpful editorial and literature suggestions, on early version of the manuscript. The initial code development work of K.N., performed during December 2013 to August 2014, was funded by the Academy of Finland through grant 267073/2013. A. Osmane and A. Dimmock were funded through 267073/2013A. Dimmock is also funded through the Academy of Finland grant 288472. Subsequent simulation work, testing of different boundary conditions and resolutions, plasma transport, and random phase analysis of K.N., was supported by the NSF GEM grant 1502774 and NASA grant NNX16AF89G. K.N. and C.F. acknowledge the support by the International Space Science Institute (ISSI) Team on Flow-Driven Instabilities of the Sun-Earth System. The THEMIS data are available at http://themis.ssl.berkeley.edu/index.shtml and the OMNI data at http://omniweb.gsfc.nasa.gov.

References

Belmont, G., and G. Chanteur (1989), Advances in magnetopause Kelvin-Helmholtz instability studies, *Phys. Scr.*, *40*, 124.

Berchem, J., and C. T. Russell (1982), The thickness of the magnetopause current layer: ISEE 1 and 2 observations, *J. Geophys. Res.*, *87*(A4), 2108–2114, doi:10.1029/JA087iA04p02108.

Blanco-Cano, X., N. Omidi, and C. T. Russell (2006), Macrostructure of collisionless bow shocks: 2. ULF waves in the foreshock and magnetosheath, *J. Geophys. Res.*, *111*, A10205, doi:0.1029/2005JA011421.

Chaston, C. C., M. Wilber, F. S. Mozer, M. Fujimoto, M. L. Goldstein, M. Acuna, H. Reme, and A. Fazakerley (2007), Mode conversion and anomalous transport in Kelvin-Helmholtz vortices and kinetic Alfvén waves at the Earth's magnetopause, *Phys. Rev. Lett.*, *99*(17), 175004, doi:10.1103/PhysRevLett.99.175004.

Chen, Q., A. Otto, and L. C. Lee (1997), Tearing instability, Kelvin-Helmholtz instability, and magnetic reconnection, *J. Geophys. Res.*, *102*, 151–161.
Claudepierre, S. G., S. R. Elkington, and M. Wiltberger (2008), Solar wind driving of magnetospheric ULF waves: Pulsations driven by velocity shear at the magnetopause, *J. Geophys. Res.*, *113*, A05218, doi:10.1029/2007JA012890.
Claudepierre, S. G., M. K. Hudson, W. Lotko, J. G. Lyon, and R. E. Denton (2010), Solar wind driving of magnetospheric ULF waves: Field line resonances driven by dynamic pressure fluctuations, *J. Geophys. Res.*, *115*, A11202, doi:10.1029/2010JA015399.
Cowee, M. M., D. Winske, and S. P. Gary (2009), Two-dimensional hybrid simulations of superdiffusion at the magnetopause driven by Kelvin-Helmholtz instability, *J. Geophys. Res.*, *114*, A10209, doi:10.1029/2009JA014222.
Cowee, M. M., D. Winske, and S. P. Gary (2010), Hybrid simulations of plasma transport by Kelvin-Helmholtz instability at the magnetopause: Density variations and magnetic shear, *J. Geophys. Res.*, *115*, A06214, doi:10.1029/2009JA015011.
Dimmock, A. P., and K. Nykyri (2013), The statistical mapping of magnetosheath plasma properties based on THEMIS measurements in the Magnetosheath Interplanetary Medium reference frame, *J. Geophys. Res. Space Physics*, *118*, 4963–4976, doi:10.1002/2013JA50465.
Dimmock, A. P., K. Nykyri, and T. I. Pulkkinen (2014), A statistical study of magnetic field fluctuations in the dayside magnetosheath and their dependence on upstream solar wind conditions, *J. Geophys. Res. Space Physics*, *119*, 6231–6248, doi:10.1002/2014JA020009.
Dimmock, A. P., K. Nykyri, H. Karimabadi, A. Osmane, and T. I. Pulkkinen (2015), A statistical study into the spatial distribution and dawn-dusk asymmetry of dayside magnetosheath ion temperatures as a function of upstream solar wind conditions, *J. Geophys. Res. Space Physics*, *120*, 2767–2782, doi:10.1002/2014JA020734.
Dimmock, A. P., K. Nykyri, A. Osmane, and T. I. Pulkkinen (2016), Statistical mapping of ULF Pc3 velocity fluctuations in the Earth's dayside magnetosheath as a function of solar wind conditions, *Adv. Space Res.*, *58*, 196–207, doi:10.1016/j.asr.2015.09.039.
Dungey, J. W. (1961), Interplanetary magnetic field and the auroral zones, *Phys. Rev. Lett.*, *6*, 47–48, doi:10.1103/PhysRevLett.6.47.
Eastwood, J. P., A. Balogh, M. W. Dunlop, T. S. Horbury, and I. Dandouras (2002), Cluster observations of fast magnetosonic waves in the terrestrial foreshock, *Geophys. Res. Lett.*, *29*(22), 2046, doi:10.1029/2002GL015582.
Eastwood, J. P., A. Balogh, E. A. Lucek, C. Mazelle, and I. Dandouras (2003), On the existence of Alfvén waves in the terrestrial foreshock, *Ann. Geophys.*, *21*, 1457–1465.
Eastwood, J. P., A. Balogh, C. Mazelle, I. Dandouras, and H. Reme (2004), Oblique propagation of 30 s period fast magnetosonic foreshock waves: A cluster case study, *Geophys. Res. Lett.*, *31*, L04804, doi:10.1029/2003GL018897.
Eastwood, J. P., A. Balogh, E. Lucek, C. Mazelle, and I. Dandouras (2005), Quasi-monochromatic ULF foreshock waves as observed by the four-spacecraft cluster mission: 1. Statistical properties, *J. Geophys. Res.*, *110*, A11219, doi:10.1029/2004JA010617.
Elkington, S. R., M. K. Hudson, and A. A. Chan (1999), Acceleration of relativistic electrons via drift-resonant interaction with toroidal-mode Pc-5 ULF oscillations, *Geophys. Res. Lett.*, *26*, 3273–3276, doi:10.1029/1999GL003659.
Eriksson, S., et al. (2016), Magnetospheric multiscale observations of magnetic reconnection associated with Kelvin-Helmholtz waves, *Geophys. Res. Lett.*, *43*, 5606–5615, doi:10.1002/2016GL068783.
Faganello, M., F. Califano, F. Pegoraro, T. Andreussi, and S. Benkadda (2012), Magnetic reconnection and Kelvin-Helmholtz instabilities at the Earth's magnetopause, *Plasma Phys. Controlled Fusion*, *54*(12), 124–037.
Fairfield, D. H., A. Otto, T. Mukai, S. Kokubun, R. P. Lepping, J. T. Steinberg, A. J. Lazarus, and T. Yamamoto (2000), Geotail observations of the Kelvin-Helmholtz instability at the eqatorial magnetotail boundary for parallel northward fields, *J. Geophys. Res.*, *105*, 21,159–21,174.
Foullon, C., E. Verwichte, V. M. Nakariakov, K. Nykyri, and C. J. Farrugia (2011), Magnetic Kelvin-Helmholtz instability at the Sun, *Astrophys. J. Lett.*, *729*, L8, doi:10.1088/2041-8205/729/1/L8.
Foullon, C., E. Verwichte, K. Nykyri, M. J. Aschwanden, and I. G. Hannah (2013), Kelvin-Helmholtz instability of the CME reconnection outflow layer in the low corona, *Astrophys. J.*, *767*, 170, doi:10.1088/0004-637X/767/2/170.
Fujimoto, M., and T. Terasawa (1994), Anomalous ion mixing within an MHD scale Kelvin-Helmholtz vortex, *J. Geophys. Res.*, *99*, 8601–8614.
Fujimoto, M., T. Terasawa, T. Mukai, Y. Saito, T. Yamamoto, and S. Kokubun (1998), Plasma entry from the flanks of the near-Earth magnetotail: Geotail observations, *J. Geophys. Res.*, *103*, 4391–4408.
Hasegawa, H., M. Fujimoto, T.-D. Phan, H. Reme, A. Balogh, M. W. Dunlop, C. Hashimoto, and R. TanDokoro (2004), Transport of solar wind into Earth's magnetosphere through rolled-up Kelvin-Helmholtz vortices, *Nature*, *430*, 755–758.
Hasegawa, H., et al. (2009), Kelvin-Helmholtz waves at the Earth's magnetopause: Multiscale development and associated reconnection, *J. Geophys. Res.*, *114*, A12207, doi:10.1029/2009JA014042.
Hietala, H., E. K. J. Kilpua, D. L. Turner, and V. Angelopoulos (2014), Depleting effects of ICME-driven sheath regions on the outer electron radiation belt, *Geophys. Res. Lett.*, *41*, 2258–2265, doi:10.1002/2014GL059551.
Hwang, K.-J., M. M. Kuznetsova, F. Sahraoui, M. L. Goldstein, E. Lee, and G. K. Parks (2011), Kelvin-Helmholtz waves under southward interplanetary magnetic field, *J. Geophys. Res.*, *116*, A08210, doi:10.1029/2011JA016596.
Hwang, K.-J., M. L. Goldstein, M. M. Kuznetsova, Y. Wang, A. F. Viñas, and D. G. Sibeck (2012), The first in situ observation of Kelvin-Helmholtz waves at high-latitude magnetopause during strongly dawnward interplanetary magnetic field conditions, *J. Geophys. Res.*, *117*, A08233, doi:10.1029/2011JA017256.
Jacobs, J. A., Y. Kato, S. Matsushita, and V. A. Troitskaya (1964), Classification of geomagnetic micropulsations, *J. Geophys. Res.*, *69*, 180–181, doi:10.1029/JZ069i001p00180.
Johnson, J. R., and C. Z. Cheng (2001), Stochastic ion heating at the magnetopause due to kinetic Alfvén waves, *Geophys. Res. Lett.*, *28*, 4421–4424.
Johnson, J. R., C. Z. Cheng, and P. Song (1997), Kinetic Alfvén waves and plasma transport at the magnetopause, *Geophys. Res. Lett.*, *24*, 1423–1426.
Kavosi, S., and J. Raeder (2015), Ubiquity of Kelvin-Helmholtz waves at Earth/'s magnetopause, *Nat. Commun.*, *6*, 7019, doi:10.1038/ncomms8019.
Kepko, L., and H. E. Spence (2003), Observations of discrete, global magnetospheric oscillations directly driven by solar wind density variations, *J. Geophys. Res.*, *108*(A6), 1257, doi:10.1029/2002JA009676.
Kepko, L., H. E. Spence, and H. J. Singer (2002), ULF waves in the solar wind as direct drivers of magnetospheric pulsations, *Geophys. Res. Lett.*, *29*(8), 1197, doi:10.1029/2001GL014405.
Kilpua, E. K. J., H. Hietala, H. E. J. Koskinen, D. Fontaine, and L. Turc (2013), Magnetic field and dynamic pressure ULF fluctuations in coronal-mass-ejection-driven sheath regions, *Ann. Geophys.*, *31*, 1559–1567, doi:10.5194/angeo-31-1559-2013.
Kilpua, E. K. J., H. Hietala, D. L. Turner, H. E. J. Koskinen, T. I. Pulkkinen, J. V. Rodriguez, G. D. Reeves, S. G. Claudepierre, and H. E. Spence (2015), Unraveling the drivers of the storm time radiation belt response, *Geophys. Res. Lett.*, *42*, 3076–3084, doi:10.1002/2015GL063542.
Korotova, G. I., and D. G. Sibeck (1995), A case study of transient event motion in the magnetosphere and in the ionosphere, *J. Geophys. Res.*, *100*, 35–46, doi:10.1029/94JA02296.

Lin, D., C. Wang, W. Li, B. Tang, X. Guo, and Z. Peng (2014), Properties of Kelvin-Helmholtz waves at the magnetopause under northward interplanetary magnetic field: Statistical study, *J. Geophys. Res. Space Physics*, *119*, 7485–7494, doi:10.1002/2014JA020379.

Lyon, J. G., J. A. Fedder, and C. M. Mobarry (2004), The Lyon-Fedder-Mobarry (LFM) global MHD magnetospheric simulation code, *J. Atmos. Sol. Terr. Phys.*, *66*, 1333–1350, doi:10.1016/j.jastp.2004.03.020.

Ma, X., A. Otto, and P. A. Delamere (2014a), Interaction of magnetic reconnection and Kelvin-Helmholtz modes for large magnetic shear: 1. Kelvin-Helmholtz trigger, *J. Geophys. Res. Space Physics*, *119*, 781–797, doi:10.1002/2013JA019224.

Ma, X., A. Otto, and P. A. Delamere (2014b), Interaction of magnetic reconnection and Kelvin-Helmholtz modes for large magnetic shear: 2. Reconnection trigger, *J. Geophys. Res. Space Physics*, *119*, 808–820, doi:10.1002/2013JA019225.

Ma, X., B. Stauffer, P. A. Delamere, and A. Otto (2015), Asymmetric Kelvin-Helmholtz propagation at Saturn's dayside magnetopause, *J. Geophys. Res. Space Physics*, *120*, 1867–1875, doi:10.1002/2014JA020746.

Ma, X., A. Otto, P. A. Delamere, and H. Zhang (2016), The interaction between reconnection and Kelvin-Helmholtz in the high-latitude magnetopause, *Adv. Space Res.*, *58*, 231–239, doi:10.1016/j.asr.2016.02.025.

Mann, I. R. (1997), On the internal radial structure of field line resonances, *J. Geophys. Res.*, *102*(A12), 27,109–27,119, doi:10.1029/97JA02385.

Matsumoto, Y., and M. Hoshino (2004), Onset of turbulence induced by a Kelvin-Helmholtz vortex, *Geophys. Res. Lett.*, *31*, L02807, doi:10.1029/2003GL018195.

Matsumoto, Y., and M. Hoshino (2006), Turbulent mixing and transport of collisionless plasmas across a stratified velocity shear layer, *J. Geophys. Res.*, *111*, A05213, doi:10.1029/2004JA010988.

Matsumoto, Y., and K. Seki (2010), Formation of a broad plasma turbulent layer by forward and inverse energy cascades of the Kelvin-Helmholtz instability, *J. Geophys. Res.*, *115*, A10231, doi:10.1029/2009JA014637.

Matsuoka, H., K. Takahashi, K. Yumoto, B. J. Anderson, and D. G. Sibeck (1995), Observation and modeling of compressional Pi 3 magnetic pulsations,*J. Geophys. Res.*, *100*, 12,103–12,115, doi:10.1029/94JA03368.

McGregor, S. L., M. K. Hudson, and W. J. Hughes (2014), Modeling magnetospheric response to synthetic Alfvénic fluctuations in the solar wind: ULF wave fields in the magnetosphere, *J. Geophys. Res. Space Physics*, *119*, 8801–8812, doi:10.1002/2014JA020000.

Miura, A. (1997), Compressible magnetohydrodynamic Kelvin-Helmholtz instability with vortex pairing in the two-dimensional transverse configuration, *Phys. Plasmas*, *4*, 2871–2885, doi:10.1063/1.872419.

Miura, A., and P. L. Pritchett (1982), Nonlocal stability analysis of the MHD Kelvin-Helmholtz instability in a compressible plasma, *J. Geophys. Res.*, *87*, 7431–7444, doi:10.1029/JA087iA09p07431.

Moore, T. (2012), Identifying signatures of plasma waves and reconnection associated with Kelvin-Helmholtz activity, Ms thesis, Dep. of Phys. Sci., Embry-Riddle Aeronaut. Univ., Daytona Beach, Fla.

Moore, T. W., K. Nykyri, and A. P. Dimmock (2016), Cross-scale energy transport in space plasmas, *Nat. Phys.*, *12*, 1164–1169, doi:10.1038/NPHYS3869.

Nakamura, T. K. M., D. Hayashi, M. Fujimoto, and I. Shinohara (2004), Decay of MHD-scale Kelvin-Helmholtz vortices mediated by parasitic electron dynamics, *Phys. Rev. Lett.*, *92*(14), 145001, doi:10.1103/PhysRevLett.92.145001.

Nakamura, T. K. M., M. Fujimoto, and A. Otto (2006), Magnetic reconnection induced by weak Kelvin-Helmholtz instability and the formation of the low-latitude boundary layer, *Geophys. Res. Lett.*, *33*, L14106, doi:10.1029/2006GL026318.

Nemecek, Z., J. Safrankova, G. Zastenker, P. Pišoft, and K. Jelínek (2002), Low-frequency variations of the ion flux in the magnetosheath, *Planet. Space Sci.*, *50*(5), 567–575, doi:10.1016/S0032-0633(02)00036-3.

Nosé, M., T. Iyemori, M. Sugiura, and J. A. Slavin (1995), A strong dawn/dusk asymmetry in Pc5 pulsation occurrence observed by the DE-1 satellite, *Geophys. Res. Lett.*, *22*, 2053–2056, doi:10.1029/95GL01794.

Nykyri, K. (2013), Impact of MHD shock physics on magnetosheath asymmetry and Kelvin-Helmholtz instability, *J. Geophys. Res. Space Physics*, *118*, 5068–5081, doi:10.1002/jgra.50499.

Nykyri, K., and A. P. Dimmock (2016), Statistical study of the ULF Pc4-Pc5 range fluctuations in the vicinity of Earth's magnetopause and correlation with the low latitude boundary layer thickness, *Adv. Space Res.*, *58*, 257–267.

Nykyri, K., and C. Foullon (2013), First magnetic seismology of the CME reconnection outflow layer in the low corona with 2.5-D MHD simulations of the Kelvin-Helmholtz instability, *Geophys. Res. Lett.*, *40*, 4154–4159, doi:10.1002/grl.50807.

Nykyri, K., and A. Otto (2001), Plasma transport at the magnetospheric boundary due to reconnection in Kelvin-Helmholtz vortices, *Geophys. Res. Lett.*, *28*, 3565–3568, doi:10.1029/2001GL013239.

Nykyri, K., and A. Otto (2004), Influence of the Hall term on KH instability and reconnection inside KH vortices, *Ann. Geophys.*, *22*, 935–949, doi:10.5194/angeo-22-935-2004.

Nykyri, K., A. Otto, J. Büchner, B. Nikutowski, W. Baumjohann, L. M. Kistler, and C. Mouikis (2003), Equator-S observations of boundary signatures: FTE's or Kelvin-Helmholtz waves?, in *Earth's Low-Latitude Boundary Layer, Geophys. Monogr. Ser.*, vol. 133, pp. 205–210, AGU, Washington, D. C., doi:10.1029/133GM20.

Nykyri, K., A. Otto, B. Lavraud, C. Mouikis, L. Kistler, A. Balogh, and H. Réme (2006), Cluster observations of reconnection due to the Kelvin-Helmholtz instability at the dawn side magnetospheric flank, *Ann. Geophys.*, *24*, 2619–2643.

Osmane, A., A. P. Dimmock, R. Naderpour, T. I. Pulkkinen, and K. Nykyri (2015), The impact of solar wind ULF Bz fluctuations on geomagnetic activity for viscous timescales during strongly northward and southward IMF, *J. Geophys. Res. Space Physics*, *120*, 9307–9322, doi:10.1002/2015JA021505.

Otto, A. (1990), 3D resistive MHD computations of magnetospheric physics, *Comput. Phys. Commun.*, *59*, 185–195.

Otto, A., and D. H. Fairfield (2000), Kelvin-Helmholtz instability at the magnetotail boundary: MHD simulation and comparison with Geotail observations, *J. Geophys. Res.*, *105*, 21,175–21,190.

Paschmann, G., W. Baumjohann, N. Sckopke, T. D. Phan, and H. Lühr (1993), Structure of the dayside magnetopause for low magnetic shear, *J. Geophys. Res.*, *98*(A8), 13,409–13,422, doi:10.1029/93JA00646.

Pu, Z. Y., and M. G. Kivelson (1983), Kelvin-Helmholtz instability at the magnetopause: Solution for compressible plasmas, *J. Geophys. Res.*, *88*, 841–852, doi:10.1029/JA088iA02p00841.

Russell, C. T., and R. C. Elphic (1978), Initial ISEE magnetometer results: Magnetopause observations, *Space Sci. Rev.*, *22*, 681–715, doi:10.1007/BF00212619.

Shue, J.-H., et al. (1998), Magnetopause location under extreme solar wind conditions, *J. Geophys. Res.*, *103*, 17,691–17,700, doi:10.1029/98JA01103.

Sonnerup, B. U. O., and L. J. Cahill Jr. (1967), Magnetopause structure and attitude from Explorer 12 observations, *J. Geophys. Res.*, *72*, 171–183, doi:10.1029/JZ072i001p00171.

Taylor, M. G. G. T., et al. (2008), The plasma sheet and boundary layers under northward IMF: A multi-point and multi-instrument perspective, *Adv. Space Res.*, *41*, 1619–1629, doi:10.1016/j.asr.2007.10.013.

Taylor, M. G. G. T., et al. (2012), Spatial distribution of rolled up Kelvin-Helmholtz vortices at Earth's dayside and flank magnetopause, *Ann. Geophys.*, *30*, 1025–1035, doi:10.5194/angeo-30-1025-2012.

Verigin, M. I., et al. (2001), Analysis of the 3-D shape of the terrestrial bow shock by INTERBALL/MAGION 4 observations, *Adv. Space Res.*, *28*, 857–862, doi:10.1016/S0273-1177(01)00502-6.

Verigin, M. I., M. Tátrallyay, G. Erdős, and G. A. Kotova (2006), Magnetosheath Interplanetary medium reference frame: Application for a statistical study of mirror type waves in the terrestrial plasma environment, *Adv. Space Res.*, *37*, 515–521, doi:10.1016/j.asr.2005.03.042.

Winant, C. D., and F. K. Browand (1974), Vortex pairing: The mechanism of turbulent mixing-layer growth at moderate Reynolds number, *J. Fluid Mech.*, *63*, 237–255, doi:10.1017/S0022112074001121.

Wing, S., J. R. Johnson, P. T. Newell, and C.-I. Meng (2005), Dawn-dusk asymmetries, ion spectra, and sources in the northward interplanetary magnetic field plasma sheet, *J. Geophys. Res.*, *110*, A08205, doi:10.1029/2005JA011086.

Yan, G. Q., F. S. Mozer, C. Shen, T. Chen, G. K. Parks, C. L. Cai, and J. P. McFadden (2014), Kelvin-Helmholtz vortices observed by THEMIS at the duskside of the magnetopause under southward interplanetary magnetic field, *Geophys. Res. Lett.*, *41*, 4427–4434, doi:10.1002/2014GL060589.

Yao, Y., C. C. Chaston, K.-H. Glassmeier, and V. Angelopoulos (2011), Electromagnetic waves on ion gyro-radii scales across the magnetopause, *Geophys. Res. Lett.*, *38*, L09102, doi:10.1029/2011GL047328.